

# Measurement of the Higgs boson transverse momentum spectrum in the $WW$ decay channel at 8 TeV and first results at 13 TeV

Lorenzo Viliani  
of University of Florence

PhD Thesis



# Abstract

The cross section for Higgs boson production in pp collisions is studied using the  $H \rightarrow W^+W^-$  decay mode, followed by leptonic decays of the W bosons, leading to an oppositely charged electron-muon pair in the final state. The measurements are performed using data collected by the CMS experiment at the LHC with pp collisions at a centre-of-mass energy of 8 TeV, corresponding to an integrated luminosity of  $19.4\text{fb}^{-1}$ . The Higgs boson transverse momentum ( $p_T$ ) is reconstructed using the lepton pair  $p_T$  and missing  $p_T$ . The differential cross section times branching fraction is measured as a function of the Higgs boson  $p_T$  in a fiducial phase space defined to match the experimental acceptance in terms of the lepton kinematics and event topology. The production cross section times branching fraction in the fiducial phase space is measured to be  $39 \pm 8$  (stat)  $\pm 9$  (syst) fb. The measurements are compared to theoretical calculations based on the standard model to which they agree within experimental uncertainties.



# Contents

<b>1</b>	<b>Electroweak and QCD physics at LHC</b>	<b>3</b>
<b>2</b>	<b>The CMS experiment at the LHC</b>	<b>5</b>
2.1	The Large Hadron Collider . . . . .	5
2.2	The CMS experiment . . . . .	5
2.3	The CMS trigger system . . . . .	5
2.4	Objects definition and event reconstruction . . . . .	5
<b>3</b>	<b>Higgs boson properties in the <math>H \rightarrow WW</math> decay channel</b>	<b>7</b>
3.1	Higgs boson measurements at LHC . . . . .	7
3.2	Higgs boson measurements in the $H \rightarrow WW$ decay channel . . . . .	7
<b>4</b>	<b>Measurement of the Higgs boson transverse momentum at 8 TeV using <math>H \rightarrow WW \rightarrow 2\ell 2\nu</math> decays</b>	<b>9</b>
4.1	Introduction . . . . .	9
4.2	Datasets, Triggers and MC samples . . . . .	11
4.2.1	Datasets and triggers . . . . .	11
4.2.2	Monte-Carlo samples . . . . .	12
4.3	Analysis Strategy . . . . .	14
4.4	Event reconstruction and selections . . . . .	16
4.4.1	Event reconstruction . . . . .	16
4.4.2	Event selection . . . . .	16
4.5	Binning of the $p_T^H$ spectrum . . . . .	20
4.6	Background estimation . . . . .	22
4.6.1	$t\bar{t}$ background . . . . .	22
4.6.2	$WW$ background . . . . .	29
4.6.3	Other backgrounds . . . . .	30

4.7	Systematic uncertainties . . . . .	37
4.7.1	Background normalization uncertainties . . . . .	37
4.7.2	Experimental uncertainties . . . . .	38
4.7.3	Theoretical uncertainties . . . . .	39
4.7.4	Monte Carlo statistics . . . . .	43
4.7.5	Treatment of systematics in the shape analysis . . . . .	43
4.8	Control Plots . . . . .	44
4.8.1	Signal and background yields . . . . .	44
4.8.2	Control plots in the signal region . . . . .	44
4.9	Signal Extraction . . . . .	48
4.9.1	Fitting procedure . . . . .	49
4.10	Unfolding . . . . .	51
4.10.1	Response matrix . . . . .	52
4.10.2	Regularization method . . . . .	52
4.10.3	Closure test . . . . .	54
4.10.4	Comparison to ZZ and $\gamma\gamma$ approach . . . . .	55
4.11	Uncertainties and Unfolding . . . . .	61
4.11.1	Type A errors . . . . .	61
4.11.2	Type B errors . . . . .	62
4.11.3	Type C errors . . . . .	65
4.11.4	Combination of errors of different type . . . . .	66
4.12	Results . . . . .	73
<b>5</b>	<b>First <math>H \rightarrow WW</math> results at 13 TeV</b>	<b>79</b>
5.1	Higgs boson search at 13 TeV . . . . .	79
5.2	Search for a high mass resonance in the WW decay channel at 13 TeV . . .	79
5.3	Conclusions . . . . .	79
	Bibliography . . . . .	83







# Chapter 1

## Electroweak and QCD physics at LHC



# Chapter 2

## The CMS experiment at the LHC

### 2.1 The Large Hadron Collider

### 2.2 The CMS experiment

### 2.3 The CMS trigger system

### 2.4 Objects definition and event reconstruction



# Chapter 3

## Higgs boson properties in the $H \rightarrow WW$ decay channel

### 3.1 Higgs boson measurements at LHC

The discovery of a new boson consistent with the standard model (SM) Higgs boson has been reported by ATLAS and CMS Collaborations in 2012. The discovery has been followed by a comprehensive set of studies of properties of this new boson in several production and decay channels and no evidence of deviation from the SM expectation has been found so far. The CMS studies in the  $H \rightarrow WW \rightarrow 2\ell 2\nu$  decay channel include the measurement of the Higgs properties, as well as constraints on the Higgs total decay width and gauge bosons anomalous couplings.

### 3.2 Higgs boson measurements in the $H \rightarrow WW$ decay channel



# Chapter 4

## Measurement of the Higgs boson transverse momentum at 8 TeV using $H \rightarrow WW \rightarrow 2\ell 2\nu$ decays

### 4.1 Introduction

In this chapter the measurement of the transverse momentum spectrum of the Higgs boson, produced in proton-proton collisions at a center-of-mass energy of  $\sqrt{s} = 8 \text{ TeV}$ , is reported. This measurement can be used to directly inspect the perturbative QCD theory in the Higgs sector. In particular the  $p_T^H$  variable is sensitive to the Higgs production mode and the differential distribution in this variable can be used to inspect the effects of the top quark mass in the gluon fusion top loop. Moreover, any observed deviation from the SM expectation, especially in the tail of the  $p_T^H$  distribution, could be a hint of physics beyond the SM.

Add theoretical motivations with some plots.

Similar measurements have already been performed by CMS and ATLAS experiments in the  $ZZ$  and  $\gamma\gamma$  Higgs decay channels. The measurement reported here is the first measurement of the Higgs  $p_T$  spectrum in the  $WW$  decay channel.

The cross section has been measured in a fiducial phase space defined using generator level variables in order to mimic the experimental acceptance and reduce the systematic uncertainties on the procedure of extrapolating the results in a larger phase space.

The Higgs transverse momentum has been reconstructed calculating the vector sum of the

dilepton system transverse momentum plus missing transverse energy

$$\vec{p}_T^H = \vec{p}_T^{\ell\ell} + \vec{p}_T^{\text{miss}} \quad (4.1)$$

The signal has been extracted subtracting all backgrounds by means of a binned Maximum Likelihood fit and has been then corrected for the efficiency of the analysis selections and for the detector resolution effects using an unfolding procedure.

The differential measurement has been performed in six bins of  $p_T^H$  with variable widths, chosen to have approximately the same purity in each bin, as explained in section 4.3.



## 4.2 Datasets, Triggers and MC samples

This analysis relies on the published  $H \rightarrow WW$  measurements [1] in terms of code, selections and background estimates for both the gluon fusion (ggH) [2] and the vector boson fusion (VBF) [3] production mechanisms.

### 4.2.1 Datasets and triggers

The datasets used for the analysis correspond to  $19.4\text{fb}^{-1}$  at  $\sqrt{s} = 8$  TeV of integrated luminosity composed of the following CMS data taking periods during 2012: 2012A ( $892\text{ pb}^{-1}$ ), 2012B ( $4440\text{ pb}^{-1}$ ), and 2012C ( $6898\text{ pb}^{-1}$ ) and 2012D ( $7238\text{ pb}^{-1}$ ). Data have been checked and validated and only data corresponding to good data taking quality are considered. The  $e^\pm\mu^\mp$  final state is considered in this analysis.

For the data samples, the events are required to fire one of the unprescaled single-electron, single-muon or muon-electron triggers. A full description of these triggers is given in [4] for 8 TeV data. Although identification and isolation criteria are also applied, a brief overview of the HLT transverse momentum ( $p_T$ ) criteria on the leptons is given in Table 4.1. While the HLT lepton  $p_T$  thresholds of 17 and 8 GeV for the double lepton triggers accommodate the offline lepton  $p_T$  selection of 20 and 10 GeV, the higher  $p_T$  thresholds in the single lepton triggers help partially recovering double lepton trigger inefficiencies as a high  $p_T$  lepton is on average expected due to the kinematic of the Higgs decay.

**Table 4.1:** Highest transverse momentum thresholds applied in the lepton triggers at the HLT level. Double set of thresholds indicates the thresholds for each leg of the double lepton triggers.

Trigger Path	7 TeV	8 TeV
Single-Electron	$p_T > 27\text{ GeV}$	$p_T > 27\text{ GeV}$
Single-Muon	$p_T > 15\text{ GeV}$	$p_T > 24\text{ GeV}$
Muon-Electron	$p_T > 17\text{ and } 8\text{ GeV}$	$p_T > 17\text{ and } 8\text{ GeV}$
Electron-Muon	$p_T > 17\text{ and } 8\text{ GeV}$	$p_T > 17\text{ and } 8\text{ GeV}$

No trigger requirement is made on the simulated events but the combined trigger efficiency is estimated from data and applied as a weight to all simulated events. The

detailed trigger efficiencies and the weighting procedure can be found in Appendix C of [2] [5]. The average trigger efficiency for signal events that pass the full event selection is measured to be about 96% in the  $e\mu$  final state for a Higgs boson mass of about 125 GeV.

## 4.2.2 Monte-Carlo samples

Several Monte Carlo event generators are used to simulate the signal and background processes:

- The POWHEG program [6] provides event samples for the  $H \rightarrow WW$  signal for the gluon fusion (ggH) and VBF production mechanisms, as well as  $t\bar{t}$  and  $tW$  processes.
- The  $q\bar{q} \rightarrow WW$ , Drell-Yan,  $ZZ$ ,  $WZ$ ,  $W\gamma$ ,  $W\gamma^*$ , tri-bosons and  $W$ +jets processes are generated using the MADGRAPH 5.1.3 [7] event generator.
- The VH process is simulated using PYTHIA 6.424 [8].

For leading-order generators samples, the CTEQ6L [9] set of parton distribution functions (PDF) is used, while CT10 [10] is used for next-to-leading order (NLO) ones. Cross section calculations [**LHCHiggsCrossSectionWorkingGroup:2011ti**] at next-to-next-to-leading order (NNLO) are used for the  $H \rightarrow WW$  process (POWHEG NLO generator is tuned to reproduce NNLO accuracy on the on-shell Higgs  $p_T$  spectrum and scaled to NNLO inclusive cross-section), while NLO calculations are used for background cross sections. For all processes, the detector response is simulated using a detailed description of the CMS detector, based on the GEANT4 package [11].

Minimum bias events are superimposed on the simulated events to emulate the additional pp interactions per bunch crossing (pile-up). The number of pile-up events simulated in the MC samples (in the same bunch crossing, in time, or in the previous or following one, out of time pile-up) have been generated poissonianly sampling from a distribution similar to what is expected from data. These samples are reweighted to represent the pile-up distribution as measured in the data. For a given range of analyzed runs, the mean number of pile-up interactions per bunch crossing is estimated per luminosity block using the instantaneous luminosity provided by the LHC, integrated over the entire run range and normalized. This distribution is then used to reweight the simulated pile-up distribution. The average

number of pile-up events per beam crossing in the 2011 data is about 10, and in the 2012 data it is about 20.

The contribution of the  $t\bar{t}H$  production mechanisms was checked to be negligible in each bin of  $p_T^H$  (below 1%) and was not taken into account. In figure 4.1 is shown the relative fraction of the four different production modes in each bin of  $p_T^H$ .

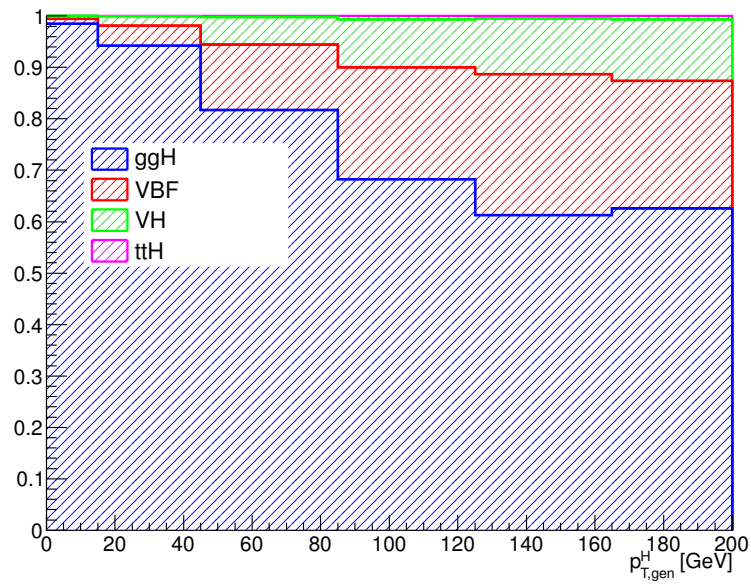


**Figure 4.1:** Relative fraction of ggH, VBF, VH and  $t\bar{t}H$  in each bin of the Higgs boson transverse momentum.

### 4.3 Analysis Strategy

The Higgs boson transverse momentum is measured in a fiducial phase space, which is defined at generator level requiring

- Exactly two status 3 leptons, an electron and a muon, originated from the  $H \rightarrow WW \rightarrow 2\ell 2\nu$  decays, with opposite charge, with  $|\eta| < 2.5$  and  $p_T > 20$  GeV and  $p_T > 10$  GeV for the leading and subleading leptons respectively.
- Generator level invariant mass of the two leptons  $m_{\ell\ell} > 12$  GeV.
- Vector sum of the two status 3 leptons  $p_T^{\ell\ell} > 30$  GeV.
- Generator level transverse mass  $\sqrt{(p_T^{\ell\ell} + p_T^{\nu\nu})^2 - (\vec{p}_T^{\ell\ell} + \vec{p}_T^{\nu\nu})^2} > 50$  GeV.

Experimentally, the Higgs boson transverse momentum is reconstructed as the vector sum of the lepton momenta in the transverse plane and MET.

$$\vec{p}_T^H = \vec{p}_T^{\ell\ell} + \vec{p}_T^{miss} \quad (4.2)$$

Compared to other differential analysis of the Higgs cross section, such as those in the  $ZZ$  and  $\gamma\gamma$  decay channels, this analysis has to cope with the limited resolution due to the  $\vec{p}_T^{miss}$  entering the transverse momentum measurement. The effect of the limited  $\vec{p}_T^{miss}$  resolution has two main implications on the analysis strategy:

- the choice of the binning in the transverse momentum spectrum needs to be reasonable when compared to the resolution. A detailed explanation of how the binning is defined is given in Sec. 4.5.
- Non negligible bin migration effects are present, and an unfolding procedure needs to be applied, not only to correct for selection efficiencies, as in  $ZZ$  and  $\gamma\gamma$ , but also to correct for bin migration effects. This is explained in Sec. 4.10.

A detailed description of the fiducial region definition and about its optimization is given in appendix ??.

The selection is essentially based on the one in the  $H \rightarrow WW \rightarrow 2\ell 2\nu$  published analysis [1] with one noticeable difference being the fact that in this analysis we do not make categories in the number of jets. The reason for this choice is that the number of jets

is strongly correlated with the transverse momentum, so making an inclusive analysis in the number of jets allows the dropping of most of the uncertainties related to the signal modeling of the number of jets produced in association with the Higgs boson. A detailed description of the selection is shown in Sec. 4.4.

The estimation of the backgrounds is different, to some extent, with respect to the one of the published  $H \rightarrow WW \rightarrow 2\ell 2\nu$ . This is mainly due to the absence of the jet binning. The techniques used to assess the backgrounds in each bin are discussed in Secs. 4.6.1, 4.6.2, 4.6.3.

Concerning the signal extraction, this analysis is again based on the already published  $H \rightarrow WW \rightarrow 2\ell 2\nu$  analysis, although we fit the signal component in each of the transverse momentum bins, using two dimensional templates in the  $m_{\ell\ell}$ ,  $m_T$  plane. The signal extraction is discussed in Sec. 4.9.

Finally an unfolding procedure is needed to extract the differential distribution in a fiducial phase space. This is discussed in detail in Sec. 4.10.

## 4.4 Event reconstruction and selections

### 4.4.1 Event reconstruction

The muons, electrons, jets and missing transverse energy ( $\vec{p}_T^{\text{miss}}$ ) reconstruction and criteria are described in details in [12]. The following criteria are only a brief summary:

- **Muons:** *GlobalMuon* (with  $\chi^2/\text{ndof} < 10$ , at least one good muon hit and at least two muon segments in different muon stations) or *TrackerMuon* (provided it satisfies the "Tracker Muon Last Station Tight" selection). Several cut-based identification criteria are applied as well as the particle flow (PF) Isolation. In 2012, the PF Isolation is replaced by an MVA algorithm.
- **Electrons:** *GSF Electons*. A MVA identification criteria is applied as well as an MVA algorithm.
- **Jets:** *Anti- $k_T$  PF jets* (with  $R=0.5$  and applying L1, L2 and L3 jet energy corrections, including Pile-Up jet corrections from Fastjet method). Only jets and  $|\eta| < 4.7$  are considered. A specific Pile-Up MVA-based rejection algorithm is applied.
- **$\vec{p}_T^{\text{miss}}$ :** The  $\vec{p}_T^{\text{miss}}$  is reconstructed the *PF Algorithm* or considering *only tracks* originating from the same vertex as the two leptons. In addition, the minimum of the projections of these two  $\vec{p}_T^{\text{miss}}$  to the closest lepton direction if they are in the same hemisphere, otherwise of their original values, is used in the analysis.

### 4.4.2 Event selection

Unlike the main  $H \rightarrow WW \rightarrow 2\ell 2\nu$  analysis, this analysis is inclusive in number of jets, so we do not have to define different jet multiplicity categories. The event selection consist of several steps. The first step is to select WW -like events applying a selection that is heavily based on the main analysis selection except for few different cuts explained below. The WW -like event preselection consists of the following set of cuts:

#### 1. Lepton preselection:

- at least two opposite-sign and opposite-flavour ( $e\mu$ ) leptons reconstructed in the event;

- 
- $|\eta| < 2.5$  for electrons and  $|\eta| < 2.4$  for muons;
  - $p_T > 20$  GeV for the leading lepton. For the trailing lepton, the transverse momentum is required to be larger than 10 GeV.
2. **Extra lepton veto:** the event is required to have two and only two opposite-sign leptons passing the lepton selection.
  3.  **$\vec{p}_T^{\text{miss}}$  preselection:** particle flow  $\vec{p}_T^{\text{miss}}$  is required to be greater than 20 GeV.
  4. **Di-lepton mass cut:**  $m_{\ell\ell} > 12$  GeV in order to reject low mass resonances and QCD backgrounds.
  5. **Di-lepton  $p_T$  cut:**  $p_T^{\ell\ell} > 30$  GeV.
  6. **projected  $\vec{p}_T^{\text{miss}}$  selection:** minimum projected  $\vec{p}_T^{\text{miss}}$  required to be larger than 20 GeV.
  7. **Transverse mass:**  $m_T^H > 60$  GeV to reject Drell-Yan to  $\tau\tau$  events.

In addition to the WW-like preselection other cuts are applied in order to reduce the top background ( $t\bar{t}$  and single-top), which is one of the main backgrounds in this final state. We operate two different selections depending on the number of jets with  $p_T > 30$  GeV in the event. This is done to suppress the top background both in the low  $p_T^H$  region, where 0-jets events have the biggest contribution, and for higher values where also larger jet multiplicity events are important. The selection for 0-jets events relies on a soft muon veto, which rejects events with non-isolated soft muons (likely belonging to b-jets), and on a soft jets (with  $p_T < 30$  GeV) anti b-tagging requirement. The latter requirement exploits the Track Counting High Efficiency tagger (TCHE) to reject soft jets that are likely to come from b quarks hadronization. These are exactly the same requirements applied in the 0-jets bin of the main analysis.

For events with a jet multiplicity greater or equal than one, we apply a different selection with respect to the main analysis. In this case we exploit the good b-tagging performances of the *JetBProbability* tagger to reject all the jets with  $p_T > 30$  GeV that are likely to come from a b quark. This jet veto relies on a cut on the *JetBProbability* tagger discriminant as has been also done in the VH ( $H \rightarrow WW \rightarrow 2\ell 2\nu$ ) analysis [13]. Any jet with a discriminant value below 1.4 is identified as a non b-jet. The analysis selection requires no b-tagged jets with  $p_T > 30$  GeV.

A cut-flow plot is reported in figure 4.2 showing the effect of each selection on top of Monte Carlo samples. In the first bin, labelled as *No cut*, no selection has been applied and the bin content correspond to the total expected number of events with a luminosity of  $19.46 \text{ fb}^{-1}$ . All the events in this bin have at least two leptons with a loose transverse momentum cut of 8 GeV. In the following bin the lepton cuts are applied, including the requirement to have two opposite-sign and opposite-flavour leptons and the extra lepton veto. Then are progressively reported all the other selections, showing the effect of each cut on backgrounds and signal. For each selection is also reported the expected signal over background ratio which after the full selection reach a maximum value around 3%.

The selection efficiency is shown in Fig. 4.3 (a). The efficiency denominator is the number of events that pass the acceptance, while the numerator is the number of events that pass both the selection and the acceptance, in each  $p_T^H$  bin. The fake rate, defined by the ratio of signal events that pass the selection but are not within the acceptance, divided by the total number of events passing both the selection and the acceptance is shown in Fig. 4.3 (b). For both the selection efficiency and the fake rate the signal samples included correspond to the  $ggH$ ,  $VBF$  and  $VH$  production mechanisms. The overall efficiency and

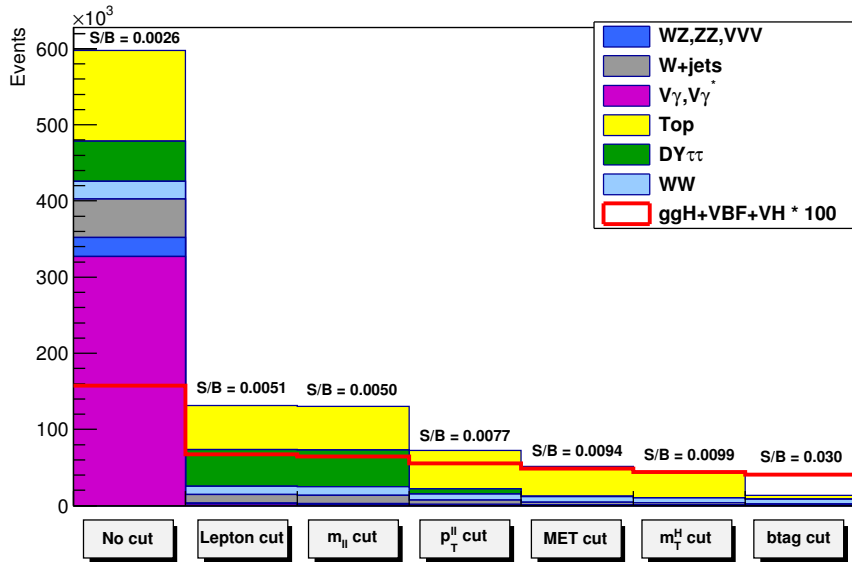


**Figure 4.2:** Effect of single selections on MC samples. The signal (red line) is multiplied by 100 and superimposed on stacked backgrounds. In each bin, corresponding to a different selection, is reported the expected number of events in MC at a luminosity of  $19.46 \text{ fb}^{-1}$ .



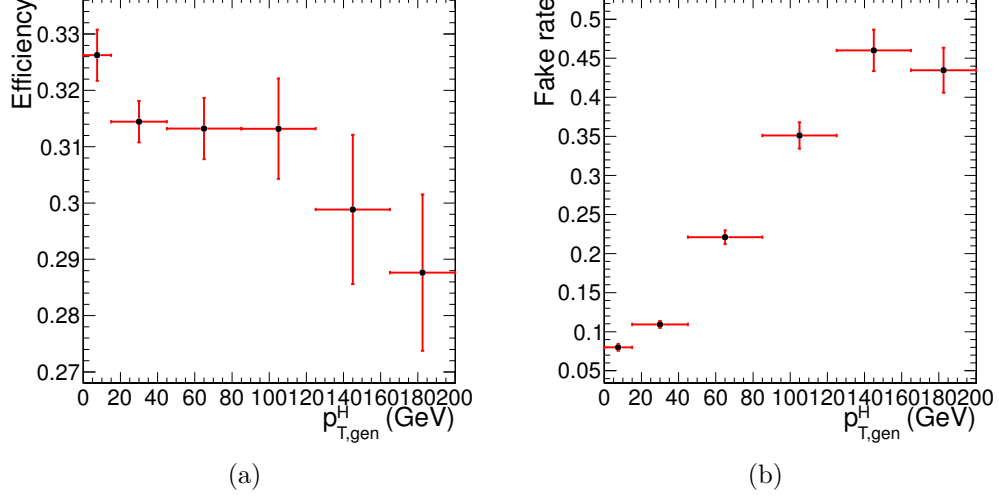


**Figure 4.3:** Efficiency of the full selection (a) and fake rate (b) as a function of  $p_T^H$ .

fake rate are:  $\epsilon = 0.362 \pm 0.005$  and  $fake\ rate = 0.126 \pm 0.004$ , where the errors are only statistical.

If we define a  $4\pi$  acceptance, requiring just that the Higgs decays to  $WW$  and then to  $2l2\nu$ , the efficiency is  $\epsilon = 0.03960 \pm 0.00033$ .

## 4.5 Binning of the $p_T^H$ spectrum

Given the limited resolution on  $p_T^H$ , a criterion is needed to establish bin size. The criterion that we have chosen is devised to keep under control the bin migrations due to the finite resolution. For any given bin  $i$  we can define the purity  $P_i$  on a signal sample as the number of events that are generated and also reconstructed in that bin,  $N_i^{GEN|RECO}$ , divided by the number of events reconstructed there  $N_i^{RECO}$ :

$$P_i = \frac{N_i^{GEN|RECO}}{N_i^{RECO}} \quad . \quad (4.3)$$

Where  $N_i^{GEN|RECO}$  is the number of events that are both generated and reconstructed in a  $p_T^H$  bin  $i$ , while  $N_i^{RECO}$  is the number of events that are reconstructed in bin  $i$ . We have chosen the bin width in such a way as to make the smallest bins able to ensure a purity of about 60% on a gluon fusion sample. Following this prescription we have divided the whole  $p_T^H$  range in six different bins: [0-15 GeV], [15-45 GeV], [45-85 GeV], [85-125 GeV], [125-165 GeV], [165- $\infty$  GeV]. A two-dimensional histogram has been made putting the GEN level  $p_T^H$  on the x-axis (calculated using the WW system transverse momentum) and the RECO one on the y-axis. Each row is then normalized to one in order to directly have the purity in the diagonal bins. Also the effect of bin migration due to finite detector resolution effects can be assessed from this plot.

This two dimensional plot is shown in Fig. 4.4 (a) and (b) for gluon fusion and VBF signals for  $m_H = 125$  GeV.

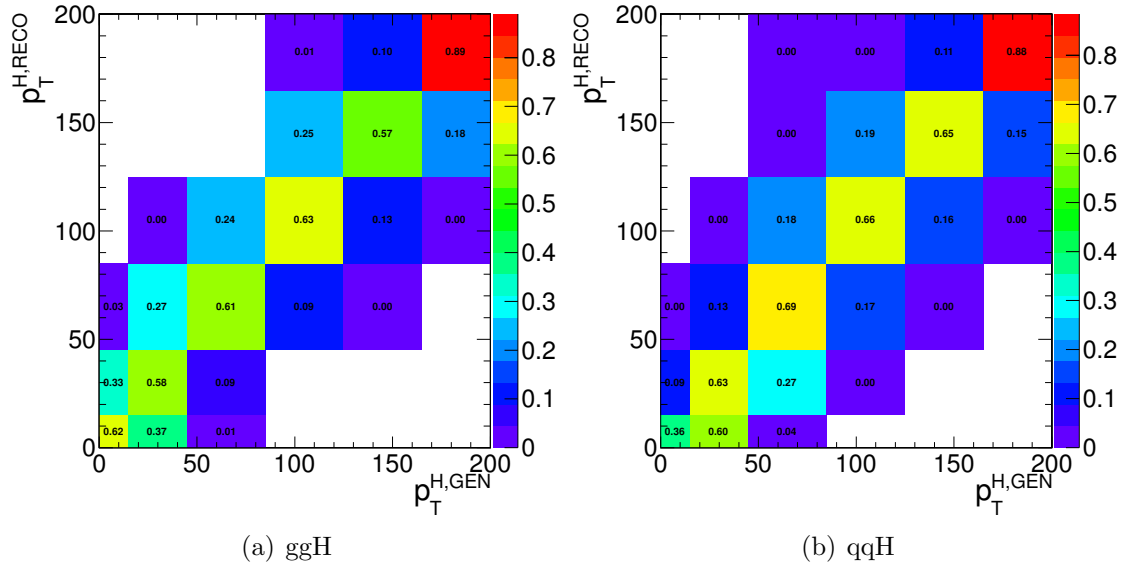


**Figure 4.4:** Reconstructed versus generated  $p_T^H$  for gluon fusion (a) and VBF (b). Plots are normalized by rows, so that the bin purity is shown on the diagonal.

## 4.6 Background estimation

Add plots for each background process

### 4.6.1 $t\bar{t}$ background

In this analysis the top background is divided into two different categories depending on the number of jets in the event. For 0-jets events we use the main analysis selections, thus also the top background estimation is the same. For events with more than 0 jets different cuts with respect to the main analysis are applied and the estimation of the top background is performed exploiting a Tag&Probe technique, explained in details later.

#### 0-jets bin

The general strategy for determining the residual top events in the signal region is to first measure the top tagging efficiencies from an orthogonal region of phase space in data. Then, using this efficiency, propagate from the control region defined as the inversion of one of the top rejection cuts. The number of surviving top events would then be:

$$N_{b\text{veto}}^{\text{signal}} = N_{b\text{tag}}^{\text{control}} \cdot \frac{1 - \epsilon_{\text{top}}}{\epsilon_{\text{top}}} \quad (4.4)$$

where  $N_{b\text{tag}}^{\text{control}}$  is the number of events in the inverted control region and  $\epsilon_{\text{top}}$  is the efficiency as measured in data. A full description of the method can be found in [2].

The amount of  $tW$  and  $t\bar{t}$  backgrounds contaminating the signal phase space is evaluated in a region obtained inverting the b-veto requirement on jets, and then extrapolated to the signal region.

#### Greater than 0-jets bin

The strategy for the estimation of the top background in events with at least one jet with  $p_T$  greater than 30 GeV is the following. We first estimate a per jet scale factor for the

b-tagging efficiency. This evaluation is performed in a control region, that we will call CtrlTP, containing at least two jets, using a Tag&Probe technique. The procedure to extract these scale factors is presented in Sec. 4.6.1. Then we define a larger statistics control region, CtrlDD, by requiring at least one b-tagged jet and we use the simulation, corrected for the previously computed b-tagging efficiency scale factor, to derive the factor that connects the number of events in CtrlDD to the number of events in the signal region. This second step is explained in detail in Sec. 4.6.1.

## Tag&Probe

The Tag&Probe technique is a method to estimate the efficiency of a selection on data. It can be applied whenever one has two objects in one event, by using one of the two, the *tag*, to identify the process of interest, and using the second, the *probe*, to actually measure the efficiency of the selection being studied. In our case we want to measure the b-tagging efficiency, so what we need is a sample with two b-jets per event. The easiest way to construct such a sample is to select  $t\bar{t}$  events.

We define a control region, called CtrlTP, which contains events passing the lepton preselection cuts listed in Sec. 4.4.2, and have at least two jets with  $p_T$  greater than 30 GeV. One of the two leading jets is required to have a *JetBProbability* score higher than 0.5. From events in this control region we built *tag-probe* pairs as follows. For each event the two leading jets are considered. If the leading jet passes the *JetBProbability* cut of 0.5, that is considered a *tag*, and the sub-leading jet is the *probe*. In order to avoid any bias that could arise from the probe being always the second jet, the pair is tested also in reverse order, meaning that the sub-leading jet is tested against the *tag* selection, and in case it passes, then the leading jet is used as *probe* in an independent *tag-probe* pair. This means that from each event passing the CtrlTP cuts one can build up to two *tag-probe* pairs.

If the *tag* selection were sufficient to suppress any non top events, one could estimate the efficiency by dividing the number of *tag-probe* pairs in which the *probe* passes the analysis cut *JetBProbability* > 1.4 (*tag-pass-probe*) by the total number of *tag-probe* pairs. However this is not the case. In order to estimate the efficiency in the presence of background we have chosen a variable that discriminates between true b-jets and other jets in a  $t\bar{t}$  sample. The variable is the  $p_T$  of the *probe* jet. For real b-jets this variable has a peak around 60 GeV, while it does not peak for other jets. The idea is to fit simultaneously the  $p_t$  spectrum

for *probe* jets in *tag-pass-probe* and *tag-fail-probe* pairs, linking together the normalizations of the two samples as follows:

$$N_{TPP} = N_s \epsilon_s + N_b \epsilon_b \quad (4.5)$$

$$N_{TFP} = N_s(1 - \epsilon_s) + N_b(1 - \epsilon_b) \quad (4.6)$$

where  $N_{TPP}$  is the number of *tag-pass-probe* pairs,  $N_{TFP}$  is the number of *tag-fail-probe* pairs,  $N_s$  is the number of *tag-probe* pairs in which the probe is a b-jet,  $N_b$  is the number of *tag-probe* pairs in which the probe is a not b-jet,  $\epsilon_s$  is the b-tagging efficiency,  $\epsilon_b$  is the probability of identifying as b-jet a non-b-jets, i.e. the mistag rate.

We have performed a  $\chi^2$  simultaneous fit of the *probe*  $p_T$  spectrum for *tag-pass-probe* and *tag-fail-probe* pairs, deriving the shapes for true b-jets and non-b-jets from the simulation, and extracting from the fit  $N_s$ ,  $N_b$ ,  $\epsilon_s$  and  $\epsilon_b$ . The result of the fit on MC simulation is shown in Fig. 4.5. The relevant efficiencies are:

$$\epsilon_s^{MC} = 0.7663 \pm 0.0072 \quad (4.7)$$

$$\epsilon_b^{MC} = 0.208 \pm 0.015 \quad (4.8)$$

We have checked that these values are consistent with the true value for the b-tagging efficiency. The true value is computed by selecting jets that are matched within a cone of  $\Delta R < 0.5$  with a generator level b-quark, and counting the fraction of those that pass the *JetBProbability* cut of 1.4. This means that the *tag-probe* method does not introduce biases within the MC statistic accuracy.

In order to assess the robustness of the fit we have generated 5000 toy MC samples and fitted them. The toy MC were generated with a statistics equivalent to the one expected in data. All the 5000 fit succeeded, and the pull distributions for  $\epsilon_s$  and  $\epsilon_b$  parameters are shown in Fig. 4.6. The pulls are well centered on 0 and have  $\sigma$  close to 1, as expected. An example fit for one of the toys is shown in Fig. 4.7

Before running the fit on data we have tried to validate the shapes used in the fit with data. To do so, we have made a much more pure  $t\bar{t}$  selection, by requiring exactly two jets

with *JetBProbability* score higher than 1.5 and no additional b-tagged jets, even if they have  $p_T$  smaller than 30 GeV. On this purer sample we have compared data against the shape used to fit the true b-jets in the *tag-pass-probe* distribution. The result is shown in Fig. 4.8 and shows good agreement.

We have finally performed the fit on data, as shown in Fig. 4.9, which results in the following efficiencies:

$$\epsilon_s^{Data} = 0.769 \pm 0.022 \quad (4.9)$$

$$\epsilon_b^{Data} = 0.121 \pm 0.054 \quad (4.10)$$

Further checks on the Tag&Probe efficiencies are shown in Appendix ??, which concern the uncertainty related to the not perfect knowledge of the  $tW/t\bar{t}$  ratio in the MC.

### Data driven estimation

In addition to the b-tagging efficiency, the other ingredient to estimate the  $t\bar{t}$  background is the process cross section. The idea is to measure the cross section in a  $t\bar{t}$  enriched control region, that we call CtrlDD. CtrlDD is defined according to the lepton preselection cuts defined in Sec. 4.4.2, and requiring in addition at least one jet with *JetBProbability* score higher than 1.4.

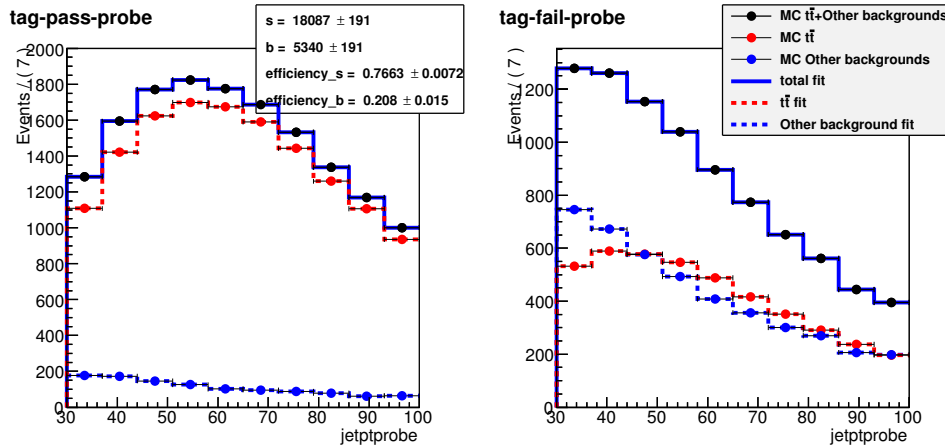


**Figure 4.5:** Simultaneous fit of the *tag-pass-probe* and *tag-fail-probe* pairs in the MC.

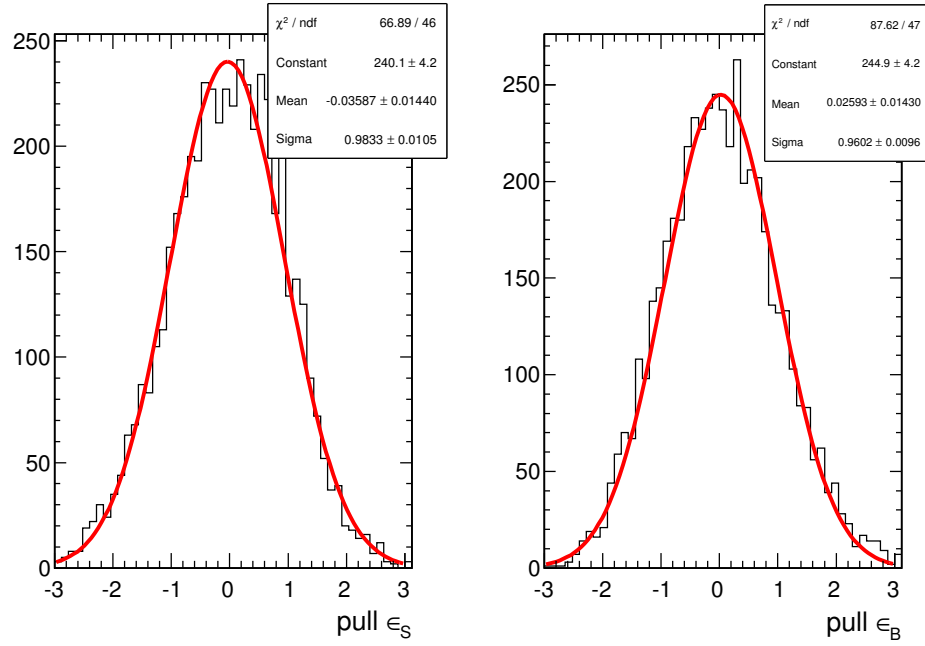


**Figure 4.6:** Pulls of the  $\epsilon_s$  and  $\epsilon_b$  parameters in 5000 toy MC.

From the simulation we derive the factor  $\alpha$  that connects CtrlIDD to the signal region, from the ratio of  $t\bar{t}$  events in the two regions.

$$\alpha = \frac{N_{t\bar{t} \text{ MC}}^{SIG}}{N_{t\bar{t} \text{ MC}}^{CtrlIDD}}. \quad (4.11)$$

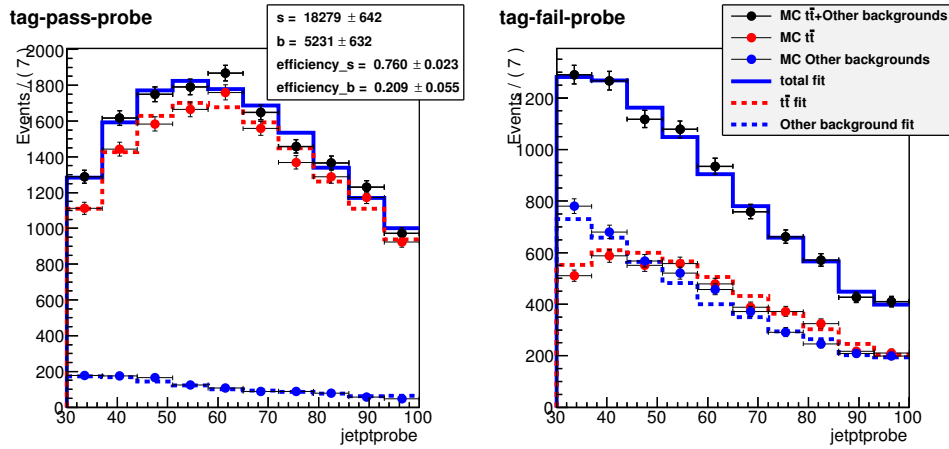


**Figure 4.7:** Fit of a toy MC sample.



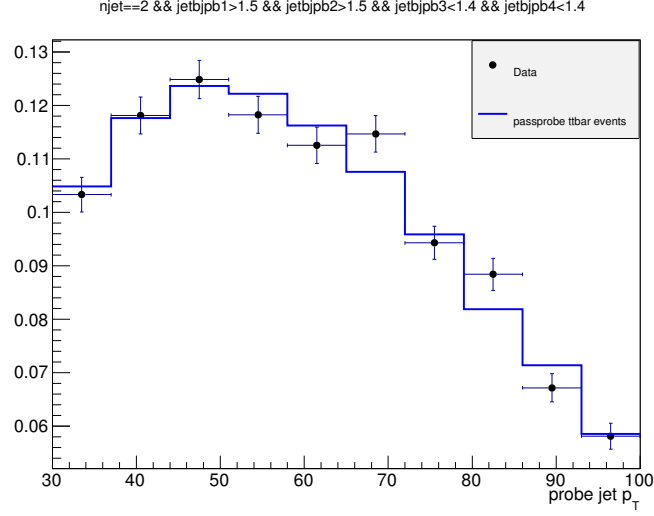


**Figure 4.8:** Shape comparison for the *probe*  $p_T$  spectrum in data and in MC in a very pure  $t\bar{t}$  sample.

We then count events CtrlDD in data, we subtract the expected number of events from non- $t\bar{t}$  backgrounds, and we obtain  $N_{t\bar{t} \text{ Data}}^{CtrlDD}$ . We finally obtain the number of expected  $t\bar{t}$  events in the signal region ( $N_{t\bar{t} \text{ Data}}^{SIG}$ ) as:

$$N_{t\bar{t} \text{ Data}}^{SIG} = \alpha N_{t\bar{t} \text{ Data}}^{CtrlDD}. \quad (4.12)$$

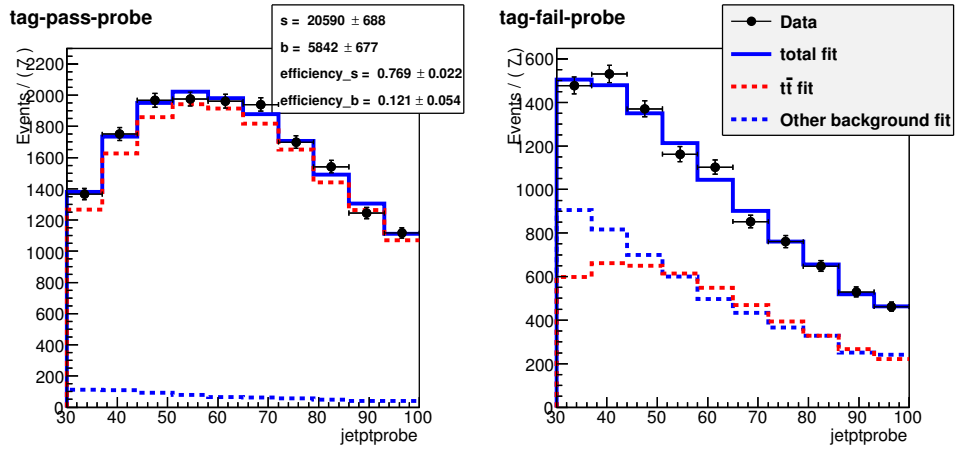


**Figure 4.9:** Simultaneous fit of the *tag-pass-probe* and *tag-fail-probe* pairs in data.

In evaluating  $\alpha$  and its error we made use of the b-tagging efficiencies determined in Sec. 4.6.1. For each event we derive an efficiency scale factor and a mistag rate scale factor, depending on whether the event is in the signal or CtrlDD regions.

$$SF_{SIG} = \left( \frac{1 - \epsilon_s^{Data}}{1 - \epsilon_s^{MC}} \right)^{\min(2, n_{b-jets})} \left( \frac{1 - \epsilon_b^{Data}}{1 - \epsilon_b^{MC}} \right)^{n_{non-b-jets}} \quad (4.13)$$

$$SF_{CtrlDD} = \left( \frac{\epsilon_s^{Data}}{\epsilon_s^{MC}} \right)^{(jet1 == b-jet)} \left( \frac{\epsilon_b^{Data}}{\epsilon_b^{MC}} \right)^{(jet1 == non-b-jets)} \quad (4.14)$$

where  $n_{b-jets}$  is the number of true b-jets in the event and  $n_{non-b-jets}$  is the number of non-b-jets in the event. The writing  $jet1 == b-jet$  ( $jet1 == non-b-jets$ ) is a boolean flag that is true when the leading jet, the one used for the CtrlDD selection, is (not) a true b-jet.

Since the efficiency and mistag rate that we have measured on data are close to the one in the MC we have decided to assume a scale factor of 1 for both b-tagging efficiency and mis-tag rate. This means that the central values of the scale factors defined in Eq. 4.13 and Eq. 4.14 is 1, but these numbers have an error that is derived assuming an uncertainty on  $\epsilon_s^{Data}$  and  $\epsilon_b^{Data}$  that covers both the statistical error from the fit of the two quantities and the difference with respect to the MC. This results in an up variation and a down variation of the scale factors in the signal region and CtrlDD regions, that is used to derive an error on  $\alpha$ .

We have decided to make a data driven estimation of the  $t\bar{t}$  background with the method described above in each of the  $p_T^H$  bins independently. The reason why we have chosen to make this estimation in  $p_T^H$  bins, rather than inclusively is explained in Fig. 4.10. In this plot the  $t\bar{t}$  background is normalized to the cross section measured by CMS. The binning is the same chosen for the analysis. As shown in the ratio plot, an overall normalization factor would not be able to accommodate for the variations of the Data/MC ratio from bin to bin.

The  $\alpha$  factors for each bin and the number of events in signal, CtrlDD region in MC as well as in data are listed in Tab. 4.2.

$p_T^H$ bin	$N_{CTRL}^{DATA}$	$N_{CTRL}^{TOP}$	$N_{SIG}^{TOP}$	$\alpha$	$\Delta\alpha$
1	406.71	358.78	117.83	0.328	0.075
2	2930.14	2703.44	859.08	0.318	0.071
3	5481.02	5207.48	1506.05	0.289	0.065
4	4126.35	4032.56	861.22	0.214	0.052
5	1612.64	1654.27	304.69	0.184	0.055
6	647.50	760.37	201.70	0.265	0.147

**Table 4.2:** Table of data driven scale factors.

A comparison of the  $m_{\ell\ell}$  distribution in the six  $p_T^H$  bins used in the analysis in CtrlDD after the data driven correction is shown in Fig. 4.11

#### 4.6.2 WW background

For what the WW background shape is concerned the prediction from the Monte-Carlo simulation has been used. This background is divided into six different parts, corresponding to the six bins of  $p_T^H$  considered. In each bin the normalization of the WW background is left free to float and is thus adjusted to match the data by the fit. In this way we minimize an effect that has been observed also in [14], that is a difference in shape between the  $p_T^{WW}$  theory prediction and the distribution provided by the MC simulation, in our case by

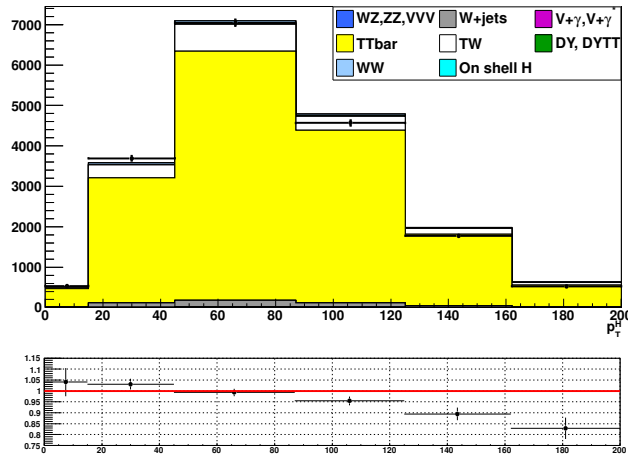


**Figure 4.10:**  $p_T^H$  variable in the CtrlDD control region.

MADGRAPH.

In figure 4.12 a comparison is shown between the  $p_T^{WW}$  spectra of two different qqWW samples: the blue line corresponds to the WW MADGRAPH samples that we use in this analysis and the red line refers to the same sample in which a reweighting has been applied in order to match the theoretical prediction at NLO+NNLL precision. A shape discrepancy can be clearly observed and the effect becomes larger at high values of  $p_T^H$ .

In order to assess if these discrepancy has a not negligible effect on the shapes of the variables that we use for the fit,  $m_{\ell\ell}$  and  $m_T$ , we checked these distributions in every  $p_T^H$  bin, comparing several samples. In particular we compared the MADGRAPH sample used for the nominal shape, the MADGRAPH sample with NLO+NNLL reweighting, a POWHEG NLO sample and an AMC@NLO sample. The results of this comparison are shown in figures 4.13 and 4.14. The discrepancy in shape among the different models is within the statistical accuracy of the MC samples.

### 4.6.3 Other backgrounds

#### W+jets background

Backgrounds containing one or two fake leptons are estimated from events selected with relaxed lepton quality criteria, using the efficiencies for real and fake leptons to pass the tight lepton quality cuts of the analysis.

A data-driven approach, described in detail in [15] and [16], is pursued to estimate this background. A set of loosely selected lepton-like objects, referred to as the 'fakeable object' or "denominator" from here on, is defined in a sample of events dominated by dijet production. The denominator object definition used in the full 2012 data is described in [17].

To measure the fake rate we count how many fakeable objects pass the full lepton selection of the analysis, parametrized as a function of the phase space of the fakeable lepton, therefore it is extracted in bins of  $\eta$  and  $p_T$ .

The ratio of the fully identified lepton, referred as "numerator", to the fakeable objects is taken as the probability for a fakeable object to fake a lepton:

---


$$\text{Fake Rate} = \frac{\#of \text{ fully reconstructed leptons}}{\#of \text{ fakeable objects}} \quad (4.15)$$

It is then used to extrapolate from the loose leptons sample to a sample of leptons satisfying the full selection.

The details of the method implementation can be found in [2]. The systematic uncertainty is evaluated by varying the jet thresholds in the di-jet control sample, and by performing a closure test in the same-sign data sample (see [2]). In both cases it is about 36%.

### **Drell-Yan to $\tau\tau$ background**

The low  $\vec{p}_T^{\text{miss}}$  threshold in  $e\mu$  final state requires the consideration of the contribution from  $Z/\gamma^* \rightarrow \tau^+\tau^-$  that is infact estimated from data.

This is accomplished by using  $Z/\gamma^* \rightarrow \mu^+\mu^-$ -events and replacing muons with a simulated  $\tau \rightarrow l\nu_\tau\bar{\nu}_e$  decay [18].

After replacing muons from  $Z/\gamma^* \rightarrow \mu^+\mu^-$ -decays with simulated  $\tau$  decays, the set of pseudo  $Z/\gamma^* \rightarrow \tau^+\tau^-$ -events undergoes the reconstruction step.

Good agreement in kinematic distributions for this sample and a Monte Carlo based  $Z/\gamma^* \rightarrow \tau^+\tau^-$ -sample is found.

The global normalization of pseudo  $Z/\gamma^* \rightarrow \tau^+\tau^-$ -events is checked in the low  $m_T$  spectrum where a rather pure  $Z/\gamma^* \rightarrow \tau^+\tau^-$ -sample is expected.

### **ZZ, WZ and W+ $\gamma$ backgrounds**

The WZ and ZZ backgrounds are partially estimated from data when the two selected leptons come from the same Z boson. If the leptons come from different bosons the contribution is expected to be small. The WZ component is largely rejected by requiring only two high  $p_T$  isolated leptons in the event.

The  $W+\gamma^{(*)}$  background, where the photon decays to an electron-positron pair, is expected to be very small, thanks to the stringent photon conversion requirements. Since the WZ simulated sample has a generation level cut on the di-lepton invariant mass ( $m_{\ell\ell} > 12$  GeV) and the cross-section raises quickly with the lowering of this threshold, a dedicated MADGRAPH sample has been produced with lower momentum cuts on two of the three leptons ( $p_T > 5$  GeV) and no cut on the third one. The surviving contribution estimated with this sample is still very small, and since the uncertainty on the cross-section for the covered phase space is large, a conservative 100% uncertainty has been given to it. A  $k$ -factor for  $W+\gamma^*$  of  $1.5 \pm 0.5$  based on a dedicated measurement of tri-lepton decays,  $W+\gamma^* \rightarrow e\mu\mu$  and  $W+\gamma^* \rightarrow \mu\mu\mu$ , is applied [19]. The contribution of  $W+\gamma^{(*)}$  is also constrained by a closure test with same sign leptons on data, which reveals a good compatibility of the data with the expected background.

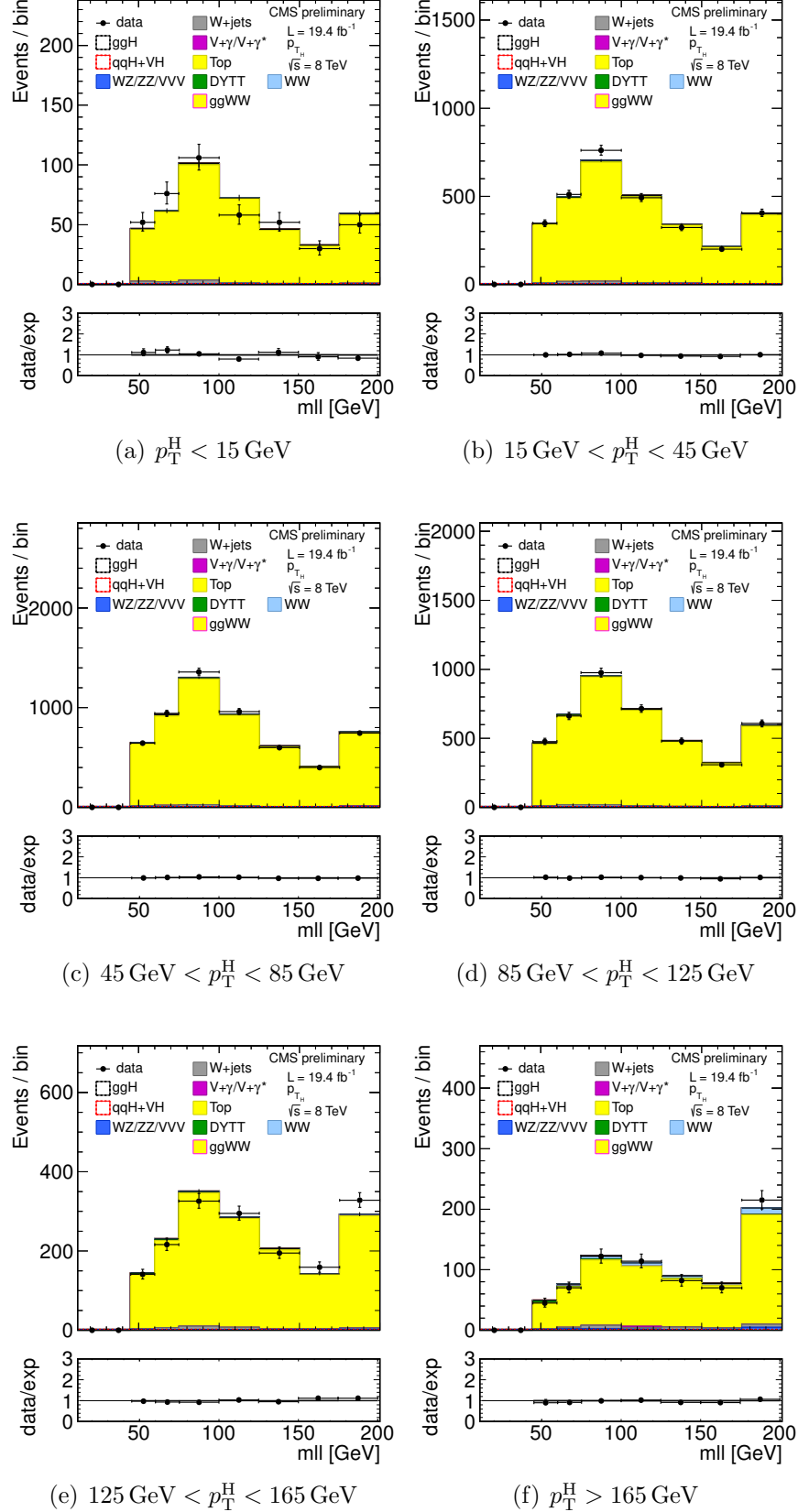


**Figure 4.11:**  $m_{\ell\ell}$  distributions in the CtrlDD region for the different  $p_T^H$  bins.

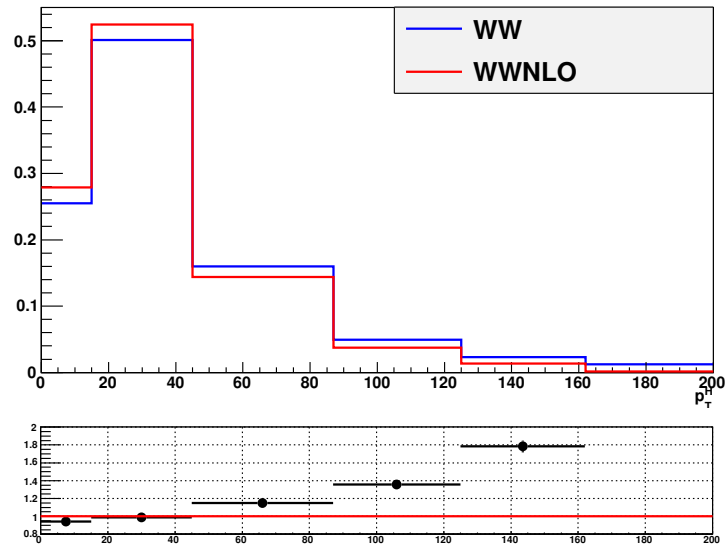
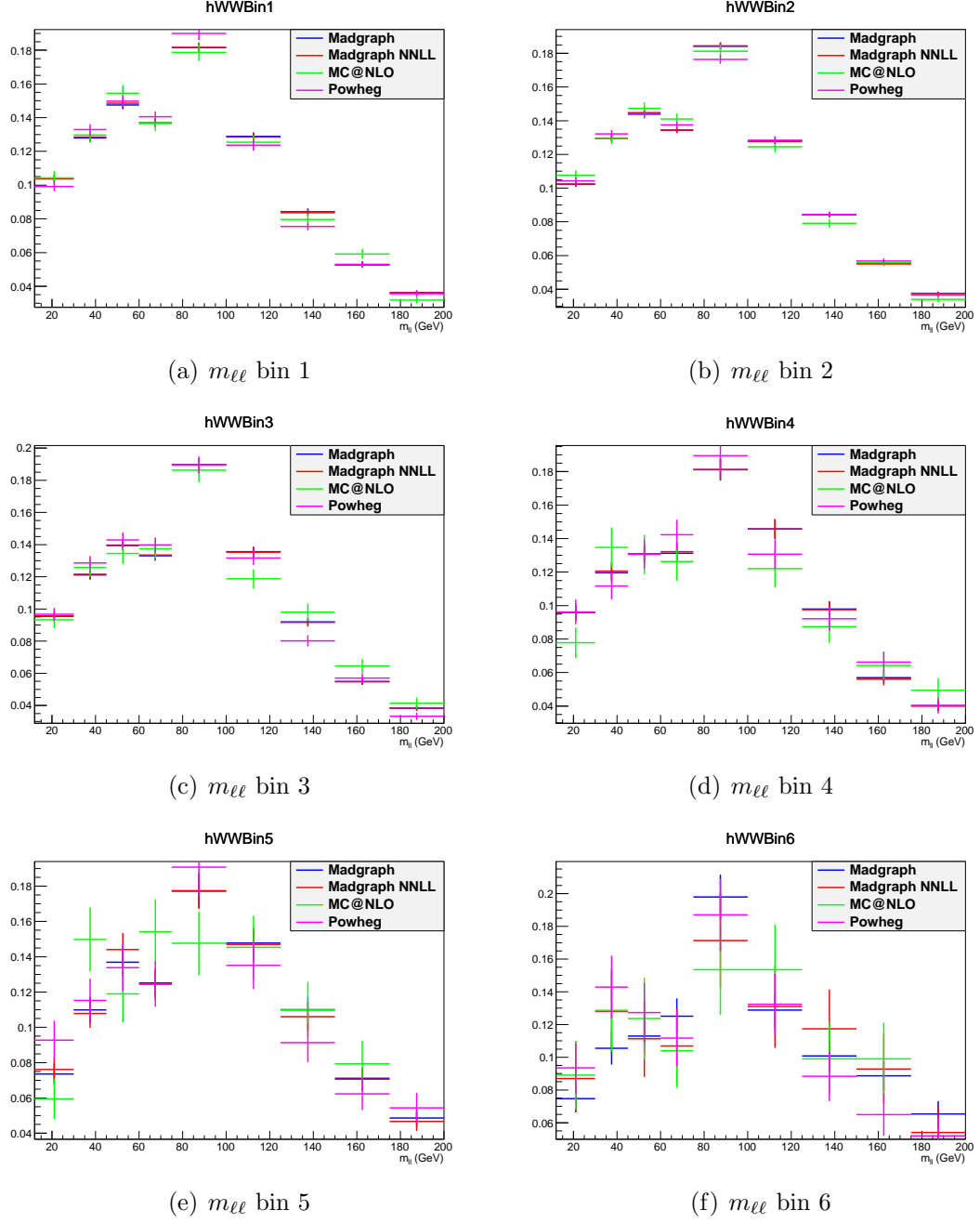
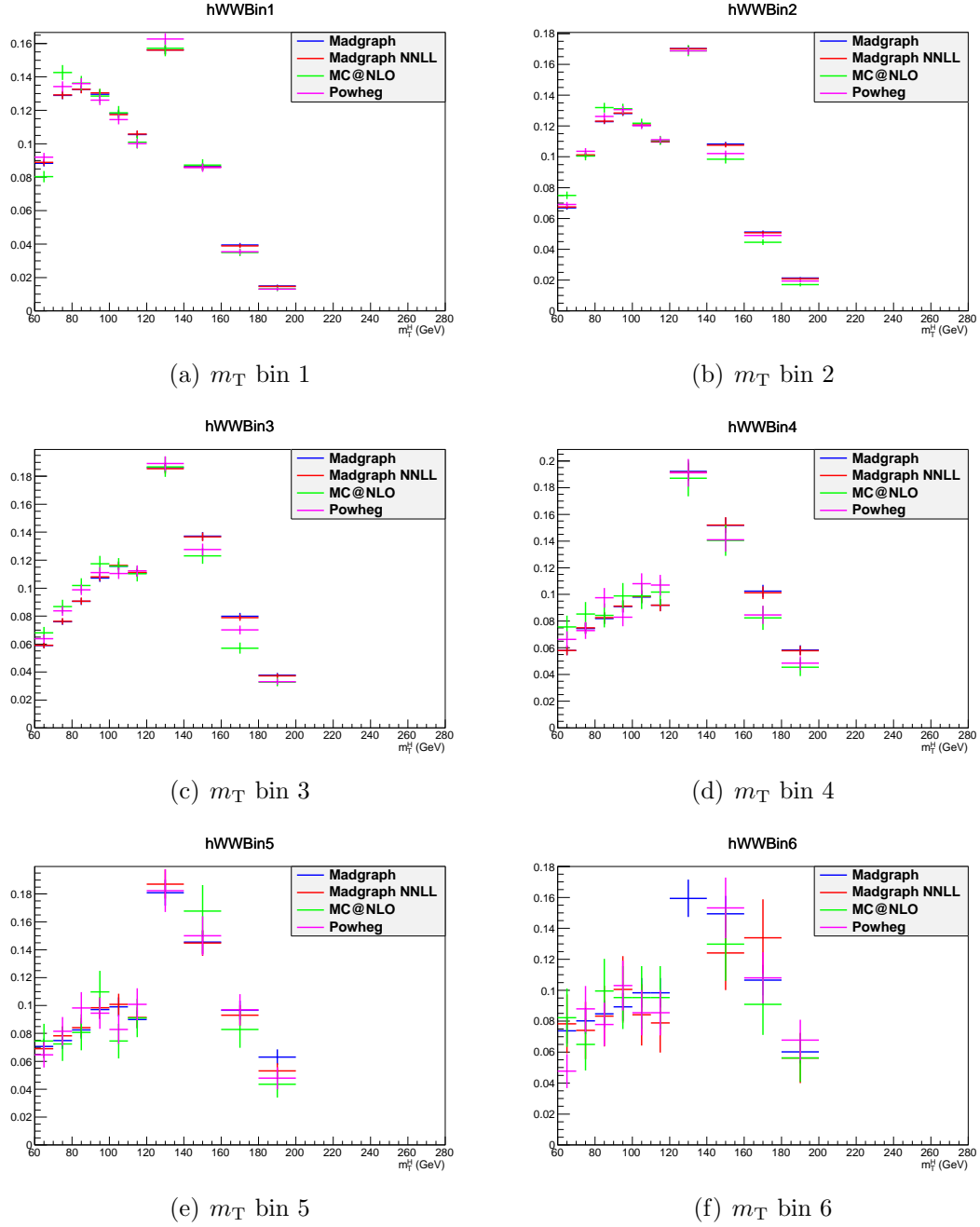


Figure 4.12





**Figure 4.13:** Comparison between the default WW background sample and other theoretical models for the  $m_{\ell\ell}$  distributions in every  $p_T^H$  bin.



**Figure 4.14:** Comparison between the default WW background sample and other theoretical models for the  $m_T$  distributions in every  $p_T^H$  bin.

## 4.7 Systematic uncertainties

Systematic uncertainties play an important role in this analysis where no strong mass peak is expected due to the presence of undetected neutrinos in the final state. One of the most important sources of systematic uncertainty is the normalization of the backgrounds that are estimated on data control samples whenever is possible.

### 4.7.1 Background normalization uncertainties

The signal extraction is performed subtracting the estimated backgrounds to the event counts in data. This uncertainty depends on the background:

- **$t\bar{t}$  and  $tW$  backgrounds:** The efficiency on jets b-tagging is estimated using the Tag&Probe technique in data and Monte Carlo control regions, as explained in 4.6.1. A per-jet scale factor, which takes into account the possibly different efficiency of the anti b-tagging selection in data and MC, is computed by means of the efficiency measured with the Tag&Probe method. The Tag&Probe method has been used also to measure the mistag rates in data and MC, which are the probability to b-tag a jet that is not produced by the hadronization of a b quark. These factors are used to reweigh the Top MC samples as explained in 4.6.1.

The uncertainties provided by the Tag&Probe fit are then propagated to the factor  $\alpha$  that is used in the top data driven estimation 4.6.1. These uncertainties are embedded in a systematic error that affects the shape of the Top background in each  $p_T^H$  bin. In fact the Top background has been splitted in six different contributions, one for each bin of  $p_T^H$ , and a different uncertainty has been associated to each background as well.

Provided that our Top MC samples include both  $t\bar{t}$  and  $tW$  processes, a systematic uncertainty related to the  $tW/t\bar{t}$  fraction has been included. In fact, a relative variation of the contribution of these two processes could modify the shape of the Top MC sample, and is thus included as a shape uncertainty affecting the Top shape in each bin of  $p_T^H$  in a correlated way.

- **$W$ +jets background:** It is estimated with data control sample as described in Sec.4.6.3. With  $19.4\text{fb}^{-1}$  at 8 TeV, the uncertainty receives similar contributions from statistics and systematic error (mainly jet composition differences between the fake

rate estimation sample and the application sample), the total error being about 40%, dominated by the closure test of the method on Monte Carlo [2].

- **WZ,ZZ,W $\gamma^{(*)}$  backgrounds:** those backgrounds, which are expected to give a small contribution, are estimated from simulation. We assign the uncertainties on cross sections reported in [20, 21]: 4% to WZ, 2.5% to ZZ. We also assign 30% on W $\gamma$  [22] and 30% on W $\gamma^{(*)}$  according to the uncertainty on the normalization study (see section 4.6.3).

### 4.7.2 Experimental uncertainties

The following experimental systematic sources have been taken into account:

- **Luminosity:** Using the online luminosity monitoring CMS reached an uncertainty on the luminosity of 2.6% at 8 TeV.
- **Trigger efficiency.** The uncertainties for both electrons and muons are at 1-2% level, which is added together to the lepton efficiency uncertainty.
- **Lepton reconstruction and identification efficiency:** The lepton reconstruction and identification efficiencies are measured with the Tag&Probe method in data. To correct for the difference in the lepton identification efficiencies between data and MC, a scale factor is applied to MC. The uncertainties resulting from this procedure on the lepton efficiencies are 4% for electrons and 3% for muons.
- **Muon momentum and electron energy scale:** The momentum scale of leptons have relatively large uncertainties due to different detector effects. For electrons a scale uncertainty of 2% for the barrel, and 4% for the endcaps respectively, is assigned. For muons, a momentum scale uncertainty of 1.5%, independent of its pseudorapidity, is assigned.
- **$\vec{p}_T^{\text{miss}}$  modeling:** The  $\vec{p}_T^{\text{miss}}$  measurement is affected by the possible mis-measurement of individual particles addressed above, as well as the additional contributions from the pile-up interactions. The effect of the missing transverse momentum resolution on the event selection is studied by applying a Gaussian smearing of 10% on the  $x$ - and  $y$ -components of the missing transverse momentum. All correlated variables, like the transverse mass, are recalculated.

- 
- **Jet energy scale (JES) uncertainties:** It affects both the jet multiplicity and the jet kinematic variables, such as  $m_{jj}$ . We estimate this uncertainty applying variations of the official jet uncertainties on the JES (which depend on  $\eta$  and  $p_T$  of the jet [23]) and compute the variation of the selection efficiency.
  - **B-mistag modeling.** A fraction of signal events is rejected because erroneously identified as b-jet by the *JetProbability* tagger. The mistag rate comes with an uncertainty due to different modeling of the b-tagging performance in data and MC. The mistag rate has been measured in data and MC with a Tag&Probe technique, as described in Sec. 4.6.1, and a per jet scale factor has been derived from the ratio of the mistag rates measured in data and MC. This scale factor is consistent with one, as shown in Sec. 4.6.1. The scale factor and its uncertainty are used to reweight each signal event with a weight corresponding to the number of non-b-jets in the event.
  - **Pileup multiplicity:** Some of the variables used in the analysis are affected by the average number of pileup interactions. The simulated events have been reweighted according the instantaneous luminosity measured on data. The error in the average number of pileup interactions measured in data and the simulation of the modeling and physics aspects of the pileup simulation gives an uncertainty of 5% on the distribution used in the reweighting procedure. This uncertainty is propagated through all the analysis, and the estimated uncertainty on the efficiency is 2%.

### 4.7.3 Theoretical uncertainties

- **Renormalization and factorization scale uncertainties:** The uncertainties on the total cross sections due to renormalization and factorization scales are assigned to MC-driven backgrounds (ggWW, WZ, ZZ). For signal these uncertainties are separated in two categories: those affecting the selection efficiency and those affecting the jet bin fractions. The effect of renormalization and factorization scales on the selection efficiency is of the order of 2% for all the processes.

Although this analysis is inclusive in number of jets we have to take into account how the QCD scales affect the jet bin migrations because of the b-tagging veto efficiency. The efficiency of this selection depends on jet multiplicity and the effect of the QCD scale variation has been evaluated using the Stewart-Tackman method, as explained in 4.7.3.

- **PDFs uncertainties:** In this analysis we have to include a nuisance taking into account the effect of PDFs on the analysis selection efficiency. Different sets of PDFs have been tested and the final effect on signal efficiency is of the order of 1%. Details can be found in the WW cross section measurement analysis note.
- **WW:** Due to the fact that the WW shape is entirely taken from Monte Carlo simulation, the analysis is strongly relying on theoretical models and can thus be strongly affected by their uncertainties. Especially higher order QCD radiation effects have an influence on the generated WW shape. To study this impact, the shapes of the distributions produced with MadGraph (which is the generator for the Monte Carlo simulation used in the analysis) are compared to the ones produced with MC@NLO. The comparison is performed separately in each bin of  $p_T^H$  and the uncertainty in each bin is always less than few percent. A comparison of the  $m_{\ell\ell}$  and  $m_T$  shapes for the WW background using different MC generators is reported in section 4.6.2.

### Jets multiplicity uncertainty

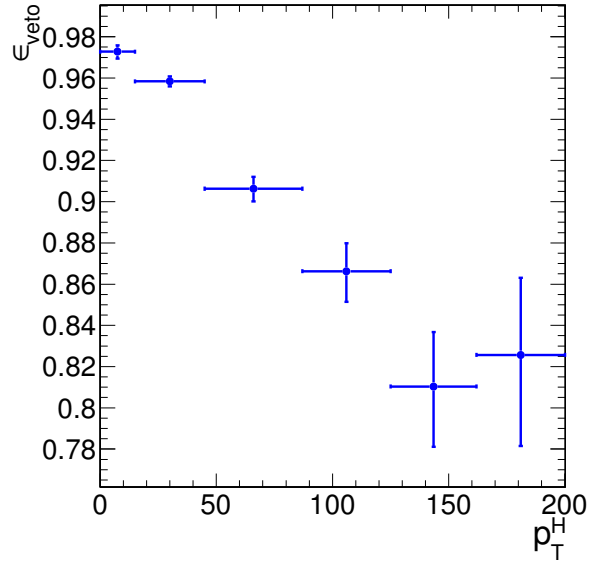
The jet bin uncertainty on ggH sample has been evaluated using the Stewart-Tackman method, following the recipe proposed in “Procedure for the LHC Higgs boson search combination” [24].

Three nuisance parameters have been calculated according to the table 4.3, where  $\kappa = \sqrt{\exp(\epsilon_-)\exp(\epsilon_+)}$  and  $\epsilon_{\pm}$  are relative QCD scale uncertainties. Exclusive cross sections for 0, 1 and 2-jet bins are calculated for the default QCD scale and their variation by changing the scale by a factor of 2 and 1/2 (up/down). The  $f_n$  constants represent the exclusive theoretical  $n$  jet bin fractions.

In this analysis, which is inclusive in number of jets, we have to include the jet binning uncertainties only if the b-tagging veto efficiency depends on the number of jets in the event. The veto efficiency has been calculated in all the  $p_T^H$  bins defined in the analysis and as a function of jets multiplicity. The results are shown in figures 4.15 and 4.16. The drop of the veto efficiency at high values of the Higgs  $p_T$  is due to the relation with jets multiplicity.

**Table 4.3:** Numerical calculation for the systematics uncertainty of jet binning.

Nuisance parameter	0-jet bin	1-jet bin	2-jet bin
QCDscale	$\kappa = (\kappa_{\geq 0})^{\frac{1}{f_0}}$		
QCDscale1in	$\kappa = (\kappa_{\geq 1})^{-\frac{f_1+f_2}{f_0}}$	$\kappa = (\kappa_{\geq 1})^{\frac{f_1+f_2}{f_1}}$	
QCDscale2in		$\kappa = (\kappa_{\geq 2})^{-\frac{f_2}{f_1}}$	$\kappa = (\kappa_{\geq 2})$

**Figure 4.15:** Efficiency of the b-tagging veto in different bins of  $p_T^H$ .

The nuisance parameters reported in table 4.3 have then been calculated for each  $p_T^H$  bin embedding the veto efficiency and using the following formulas:

$$QCDscale_{ggH} = \frac{ggH0 * f_0 * \epsilon_0 + ggH1in0 * f_1 * \epsilon_1}{ggH0 * f_0 * \epsilon_0 + ggH1in0 * f_1 * \epsilon_0} \quad (4.16)$$

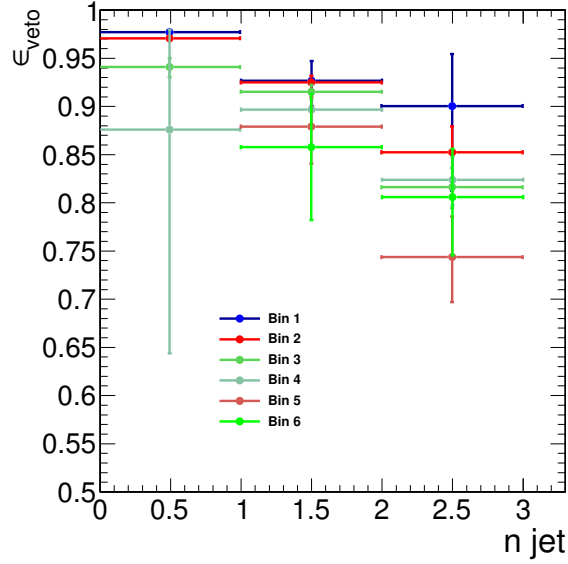


**Figure 4.16:** Efficiency of the b-tagging veto in different bins of  $p_T^H$ , as a function of number of jets.

$$QCDscale\_ggH1in = \frac{ggH1in1 * f_1 * \epsilon_1 + ggH2in1 * f_2 * \epsilon_2}{ggH1in1 * f_1 * \epsilon_1 + ggH2in1 * f_2 * \epsilon_1} \quad (4.17)$$

$$QCDscale\_ggH2in = 1 \quad (4.18)$$

These nuisance parameters are expected to be equal to one in case the efficiency is independent on the number of jets, i.e if  $\epsilon_0 = \epsilon_1 = \epsilon_2$ .

The values obtained are reported in table 4.4 divided in bins of  $p_T^H$ .

**Table 4.4:** Values of the jet binning nuisance parameters for different  $p_T^H$  bins.

	Bin 1	Bin 2	Bin 3	Bin 4	Bin 5	Bin 6
QCDscale_ggH	0.998	0.993	0.989	1.000	1.000	1.000
QCDscale_ggH1in	0.997	0.993	0.984	0.975	0.946	0.974



#### 4.7.4 Monte Carlo statistics

Due to the large range of weights to correct other MC pile up distribution to match that in data, the effective size of the MC samples are sometimes smaller than the actual number of events in the sample. The statistical uncertainty of the event yields estimated from MC samples is reflected in the final result.

#### 4.7.5 Treatment of systematics in the shape analysis

One can distinguish between normalization uncertainties, where a systematic effect is changing the normalization assuming the shape is not affected, and shape uncertainties where the actual change in the shape of the distribution is taken into account. The normalization uncertainties enter the shape analysis as a constant normalization factor, whereas for shape uncertainties the nominal and the  $+1\sigma$  and  $-1\sigma$  shapes enter the analysis in form of three histograms with the same normalization.

For the W+jets background, the shape differences for different jet  $p_T$  thresholds in the di-jet control sample are considered separately for electron and muon fakes, while the other sources of systematics are taken as normalization uncertainties as in the cut-based analysis.

Effects from experimental uncertainties are studied by applying a scaling and/or smearing of certain variables of the physics objects, followed by a subsequent recalculation of all the correlated variables. This is done for Monte Carlo simulation, to account for possible systematic mismeasurements of the data. All experimental sources from Section 4.7.2 but luminosity are treated both as normalization and shape uncertainties. For background with a data-driven normalization estimation, only the shape uncertainty is considered.

To account for statistical uncertainties, for each distribution going into the shape analysis, the  $+1\sigma$  and  $-1\sigma$  shapes were obtained by adding/subtracting the statistical error in each bin and renormalize it to the nominal distribution. In addition to this procedure a constant normalization uncertainty due to the finite statistics of the sample, used to extract the shape, is assigned.

## 4.8 Control Plots

### 4.8.1 Signal and background yields

In table 4.5 are reported the expected number of events for signals and backgrounds after the full analysis selection. The uncertainties in the expected number of events correspond to the prefit nuisances effect affecting each process. As can be observed, signals are splitted into different categories depending on the production mode: gluon fusion (ggH), VBF (qqH) and VH (WH and ZH) which includes also ttH production. Each signal is again splitted in six different contributions related to the  $p_T^H$  bins. The total expected signal yield after the analysis selection is  $382 \pm 7$  events.

For what the backgrounds are concerned, the WW has been splitted in bins of  $p_T^H$  and has been left free to float independently in each bin during the fit. For doing this a 100 % uncertainty has been associated to the expected number of events in each bin, following a prior flat distribution (log uniform distribution). That is why the uncertainty on WW backgrounds and on total background yield are not reported in the table.

The Top background has been divided into two categories of events as explained in 4.6.1: events with zero jets (Top0jet) and events with more than zero jets (Topge1jet). The yield in the first category has been extracted performing a data driven estimation in a control region. The latter category has been further splitted in the various  $p_T^H$  bins and a data driven estimation has been performed separately in each bin to avoid a shape mismodelling in the  $p_T^H$  distribution for this background.

The final signal to background ratio is around 3 %, consistent with what illustrated in figure 4.2.

### 4.8.2 Control plots in the signal region

In figure 4.17 are reported the control plots in the signal region for the  $m_{\ell\ell}$  distribution in all the  $p_T^H$  bins. Data points are superimposed to MC distributions only in the high  $m_{\ell\ell}$  region (above 70 GeV), where no signal is expected. The error bands shown in these plots correspond to the total prefit uncertainty, taking into account all the sources of error. The very large uncertainties are expected and are related to the 100 % uncertainty assigned to the WW floating background. The error band will decrease once the fit will be performed,

**Table 4.5:** Signal prediction, background estimates and observed number of events in data are shown in each  $p_T^H$  bin for the signal after applying the analysis selection requirements. The total uncertainty on the number of events is reported. For signal processes, the yield related to the ggH are shown, separated with respect to the contribution of the other production mechanisms (XH=VBF+VH). The WW process includes both quark and gluon induced contribution, while the Top process takes into account both  $t\bar{t}$  and tW.

$p_T^H$ [GeV]	0-15	15-45	45-85	85-125	125-165	165- $\infty$
ggH	$73 \pm 3$	$175 \pm 5$	$59 \pm 3$	$15 \pm 2$	$5.1 \pm 1.5$	$4.9 \pm 1.4$
XH=VBF+VH	$4 \pm 2$	$15 \pm 4$	$16 \pm 4$	$8 \pm 2$	$3.8 \pm 1.1$	$3.0 \pm 0.8$
Out-of-fiducial	$9.2 \pm 0.5$	$19.9 \pm 0.7$	$11.4 \pm 0.6$	$4.4 \pm 0.3$	$1.6 \pm 0.2$	$2.4 \pm 0.2$
Data	2182	5305	3042	1263	431	343
Total background	$2124 \pm 128$	$5170 \pm 321$	$2947 \pm 293$	$1266 \pm 175$	$420 \pm 80$	$336 \pm 74$
WW	$1616 \pm 107$	$3172 \pm 249$	$865 \pm 217$	$421 \pm 120$	$125 \pm 60$	$161 \pm 54$
Top	$184 \pm 38$	$1199 \pm 165$	$1741 \pm 192$	$735 \pm 125$	$243 \pm 51$	$139 \pm 49$
W+jets	$134 \pm 5$	$455 \pm 10$	$174 \pm 6$	$48 \pm 4$	$14 \pm 3$	$9 \pm 3$
WZ+ZZ+VVV	$34 \pm 4$	$107 \pm 10$	$71 \pm 7$	$29 \pm 5$	$14 \pm 3$	$13 \pm 4$
$Z/\gamma^* \rightarrow \tau^+ \tau^-$	$23 \pm 3$	$67 \pm 5$	$47 \pm 4$	$22 \pm 3$	$12 \pm 2$	$10 \pm 2$
$W\gamma^{(*)}$	$132 \pm 49$	$170 \pm 58$	$48 \pm 30$	$12 \pm 9$	$3 \pm 3$	$5 \pm 10$

i.e using the postfit values of the nuisance parameters, and the WW yield will be adapted to data.

As expected the Top background becomes more important while going to high values of  $p_T^H$ , accordingly to the higher jet multiplicity in that region. The discrepancy between MC prediction and data, especially for low values of Higgs  $p_T$ , is due WW background which in this plots is fixed to the MC cross section.

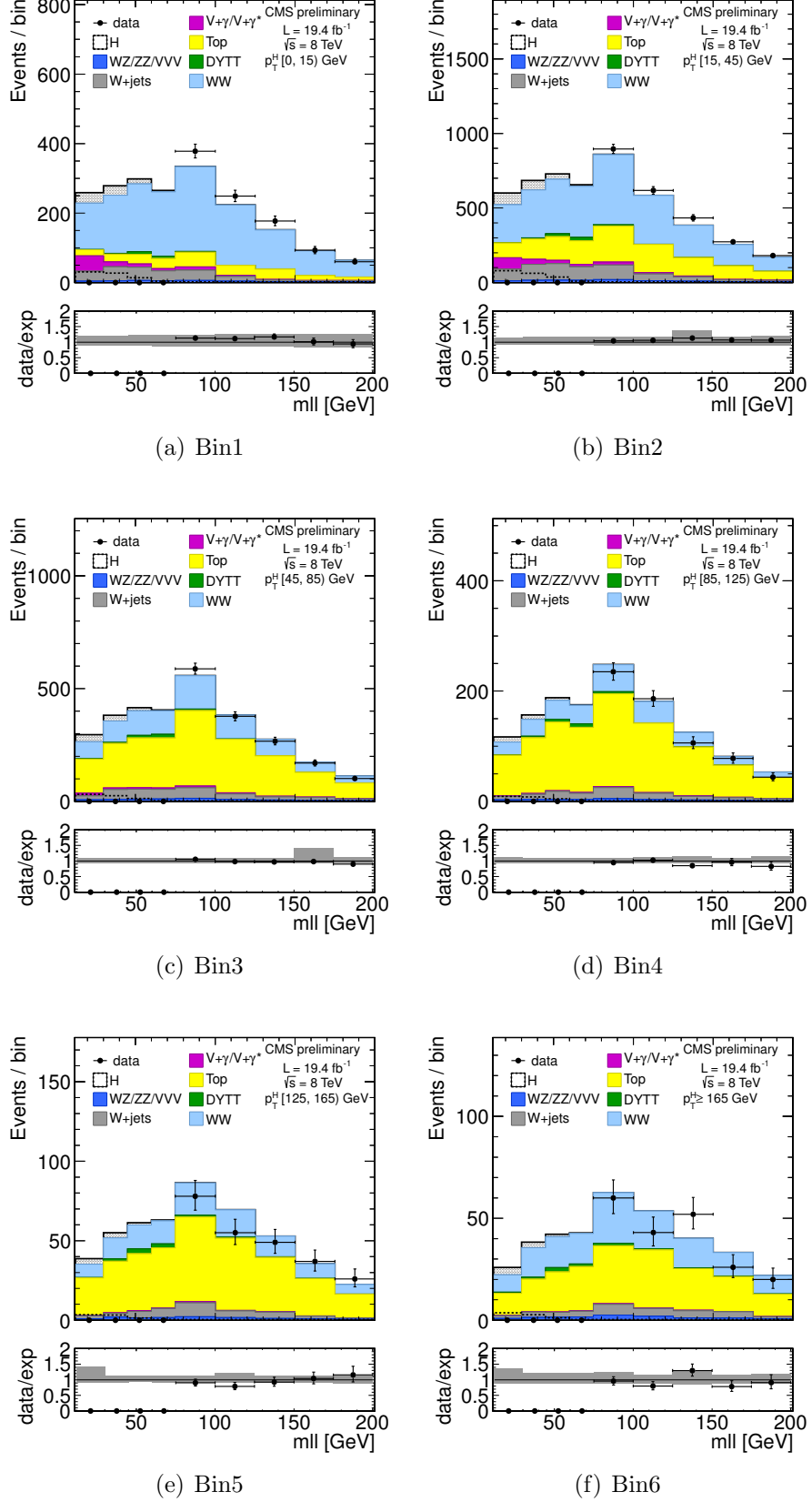


**Figure 4.17:** Control plots showing the  $m_{\ell\ell}$  distributions in every Higgs  $p_T$  bin. Data are superimposed in the region where the signal is expected to be negligible.

## 4.9 Signal Extraction

The signal is extracted in each bin of  $p_T^H$  by using a 2D template for signals and backgrounds in the  $m_{\ell\ell}$ - $m_T$  plane. This is the same strategy used in the main WW analysis. The binning of the  $m_{\ell\ell}$  and  $m_T$  templates is:

- $m_{\ell\ell}$ : [12, 30, 45, 60, 75, 100, 125, 150, 175, 200]
- $m_T$ : [60, 70, 80, 90, 100, 110, 120, 140, 160, 180, 200, 220, 240, 280]

We have checked that these two variables are not correlated with  $p_T^H$ , as shown in Fig. 4.18 and Fig. 4.19 for gluon fusion and VBF signals respectively.

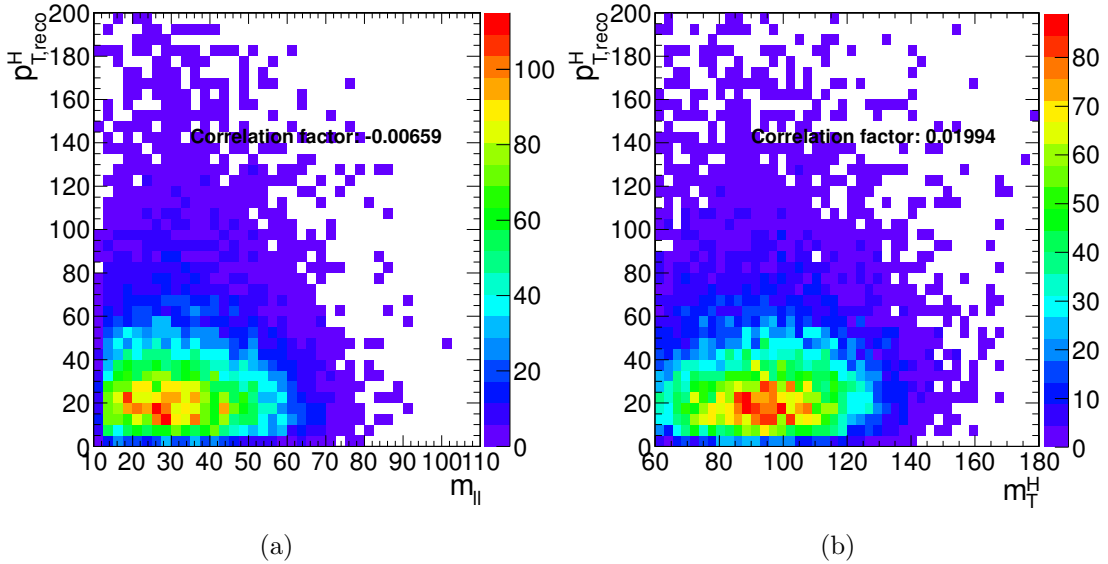


**Figure 4.18:** Correlation between  $p_T^H$  and  $m_{\ell\ell}$  (a) and between  $p_T^H$  and  $m_T$  (b) after the full selection for the gluon fusion signal.

The signal extraction is performed using the `combine` tool. We have defined a model with six signal strength parameters, one for each bin. The relative contribution for different production mechanisms in the input signal template is taken to be the same as the SM. The signal strength in each bin is allowed to float between -10 and +10, thus allowing negative values. This is mainly intended to allow the error bars to float below 0.

The fake events, i.e. reconstructed events not belonging to the fiducial region, are included in the signal definition. In fact in this step we are extracting all the events passing the analysis

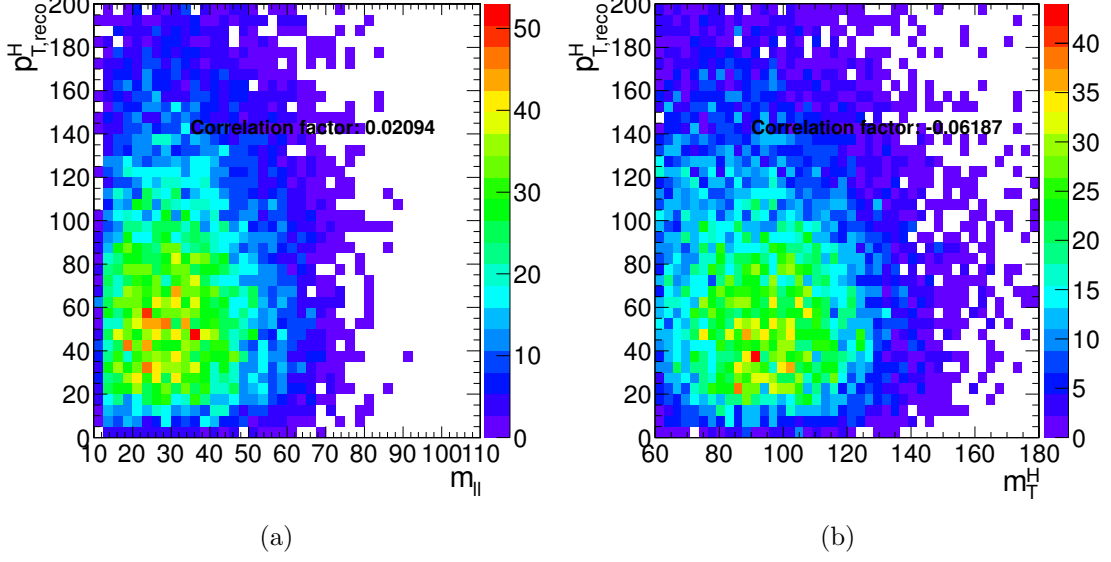


**Figure 4.19:** Correlation between  $p_T^H$  and  $m_{\ell\ell}$  (a) and between  $p_T^H$  and  $m_T$  (b) after the full selection for the VBF signal.

selection, regardless of the fiducial region definition. Those events must be subtracted before the unfolding: to do this, given the fiducial region, we have computed the expected spectrum of fake events in bins of  $p_T^H$ . Then each bin of the spectrum is multiplied by the measured signal strength in that bin and then subtracted from the measured spectrum. At the end, the number of events in each bin  $i$  of the measured spectrum is:

$$N_i = \mu_i(s_i - f_i) \quad , \quad (4.19)$$

where  $s_i$  and  $f_i$  are respectively the number of signal and fake events expected from MC and  $\mu_i$  is the measured signal strength.

#### 4.9.1 Fitting procedure

The fit is a binned likelihood fit. Each source of systematic uncertainty is represented by a nuisance parameter in the fit. Each signal is splitted in the six different bins of  $p_T^H$  as shown also in the yields table 4.5. The WW and Top backgrounds have been also splitted in the various bins of Higgs  $p_T$  in order to reduce a possible shape mismatching between data and MC.

**Table 4.6:** Best fit values and profile-likelihood uncertainties for all the signal strengths obtained fitting all the nuisances in the model.

Signal strength	Best fit value	Uncertainty (68% C.L.)
$\mu_0$	1.000	-0.408/+0.421
$\mu_1$	1.000	-0.294/+0.305
$\mu_2$	1.000	-0.420/+0.441
$\mu_3$	1.000	-0.860/+0.913
$\mu_4$	1.001	-1.224/+1.380
$\mu_5$	1.001	-0.932/+1.091

The fit is not performed on data, being the analysis is still blinded, but rather on a toy Asimov dataset. The best fit parameters values and the related profile-likelihood uncertainties extracted from the fit including all the nuisances in the model are shown in table 4.6. For each parameter of interest the MINOS algorithm has been used.

In order to assess the robustness of the fit we have also run on several toy MC with a statistics corresponding to the one expected in data. The distribution of the signal strengths extracted in each bin in the toys and the their pulls are shown in Fig. 4.20.

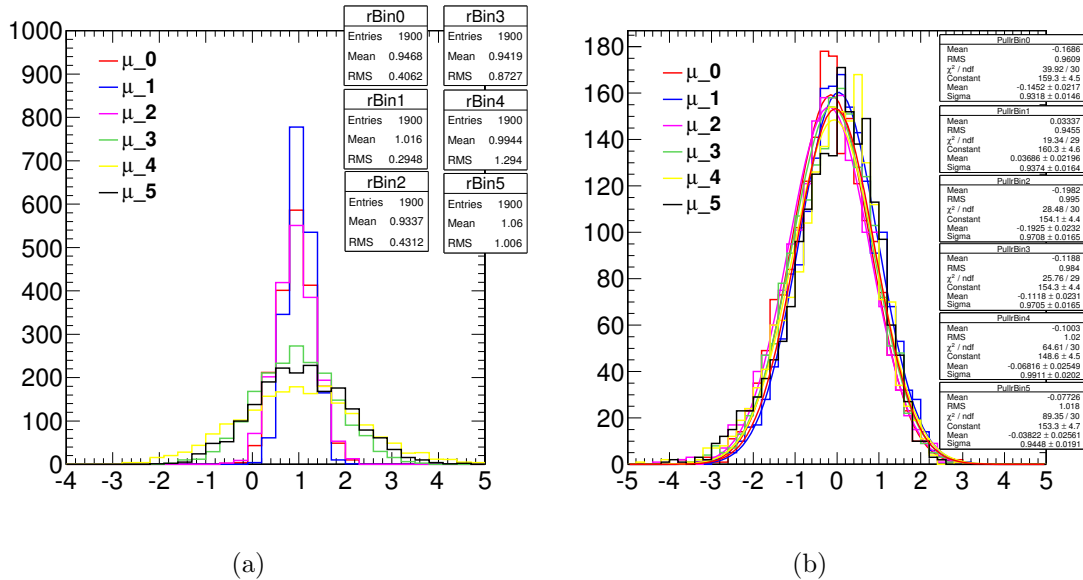


**Figure 4.20:** Signal strengths distribution as extracted from the fit in toy MC (a). Pulls of the signal strength parameters (b).



## 4.10 Unfolding

In order to report the results in such a way that is easy to make a comparison with theoretical prescriptions or with other experiments results, the signal extracted performing the fit has to be corrected for detector resolution and efficiency effects and for the efficiency of the selection defined in the analysis.

To achieve this an unfolding procedure has been set up relying on the *RooUnfold* [25] package which provides the tools to run various unfolding algorithms.

The results are extrapolated to a fiducial region defined using generator level variables, as discussed in section 4.3, in particular using the status three definition for leptons, which identifies the “hard part” of the interaction, i.e. the partons that are used in the matrix element calculation, including immediate decays of resonances. For this 8 TeV analysis, in which the uncertainty is dominated by the low statistics, the effect of unfolding to status three particles (which are, strictly speaking, not observable) instead of status one (i.e. what one would observe with a perfect detector) are expected to be negligible.

The basic principle behind the unfolding procedure is to use MC signal samples to make the “true” distribution (the one obtained with MC truth information) of the variable of interest and the same distribution obtained with events reconstructed after the full GEANT4 simulation of the CMS detector and event reconstruction. These two distributions are used to calculate the response matrix  $M$ , given by:

$$R_i^{MC} = M_{ij} T_j^{MC} \quad , \quad (4.20)$$

where  $R^{MC}$  and  $T^{MC}$  are two  $n$ -dimensional vectors (where  $n$  is the number of bins of the distribution) representing the reconstructed distribution and to the true distribution respectively.

The response  $M[n \times n]$  matrix includes all the effects related to the detector and to the analysis selection that affect the  $R^{MC}$  distribution.

The goal of the unfolding procedure is to go back to the true distribution starting from the measured one. The most natural way to achieve this would be inverting the response matrix. However it can be shown [26] that, due to the finite statistical accuracy of the response matrix, which is limited by the MC statistic, a simple inversion could lead to huge fluctuations between bins in the unfolded result. Regularization methods can however be employed to make the matrix inversion well behaved. Several methods are implemented in the *RooUnfold* package, and they all depend on the choice of a regularization parameter.

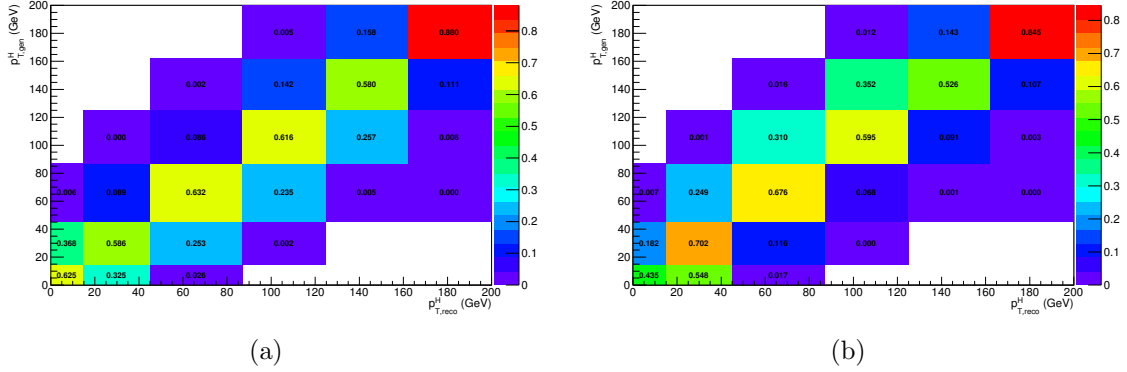


**Figure 4.21:** Response matrix normalized to one either by column (a) or by row (b).

The choice of the regularization parameter is particularly critical, and it should represent an optimal trade-off between taming the fluctuations in the unfolded result, and biasing the unfolded distribution towards the one used to build the response matrix.

#### 4.10.1 Response matrix

The first step is to build the response matrix. The matrix is built as two-dimensional histograms, plotting the generator level Higgs  $p_T$  on the  $x$  axis and the same variable at reconstructed level on the  $y$  axis. For both the generator and reconstruction level variable the same binning has been chosen following the prescription described in section 4.5. Both fake events, i.e. events reconstructed in a given bin without a generated counterpart, and miss events, i.e. events generated in a given bin but not reconstructed, are taken into account in order to build the response matrix. In figure 4.21 the response matrix is shown, either normalized by column or by row, in order to show respectively the purity and the stability values in the diagonal bins. The fake events distribution is shown in figure 4.22.

#### 4.10.2 Regularization method

In this analysis we used the SVD (Singular Value Decomposition) tool based on Tikhonov regularization function, provided within the *RooUnfold* package. The choice of the regularization parameter follows the prescription in [27]. The prescription proceeds as follows: one needs to diagonalize the response matrix with the SVD decomposition and plot, as a

function of the bin number, the values of a transformed vector called  $d_i$  which represents the measured distribution in a specific base defined by the SVD decomposition. The optimal choice for the regularization parameter is a value that corresponds to where the curve becomes flat around 1. This choice is data driven and will have to be re-evaluated after the unblinding of the data. For the moment we have performed the test on the Monte Carlo, as shown in Fig. 4.23, and we decided to use a value of 3. The test has been performed using 200 toy MC samples and calculating for each one of them the  $\log d_i$  function. The values in each bin  $i$  correspond to the mean values obtained from the toys and the corresponding errors. However, the final choice of the regularization parameter has to be done looking at data after the unblinding.

In order to show the unfolded spectrum dependence on the choice of the regularization parameter, the unfolded procedure has been repeated for several regularization values. The various plots are shown in figure 4.24 for regularization values varying from 1 (stronger regularization) to 5 (weaker regularization). Using  $k_{reg} = 6$  is equivalent to the simple inversion of the response matrix and leads to huge errors. Lowering  $k_{reg}$  means increasing the regularization and thus reducing the statistical uncertainty. One should increase the

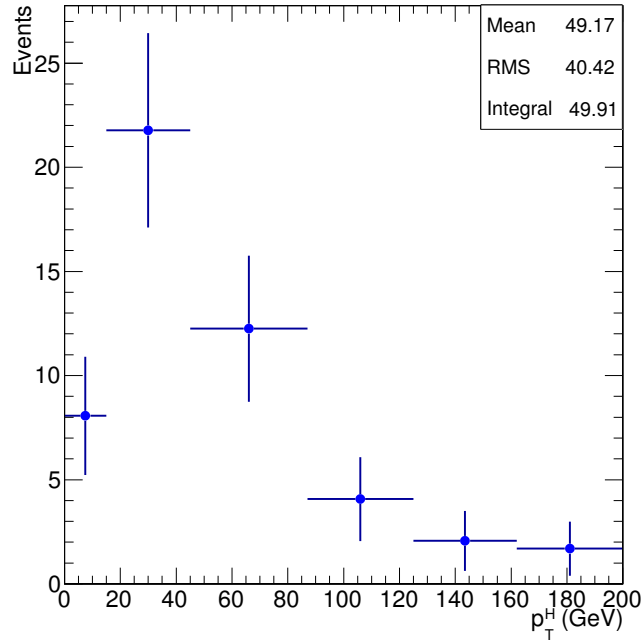


**Figure 4.22:** Fakes distribution, i.e. events reconstructed in a given bin without any generator level event associated, normalized to the data luminosity.

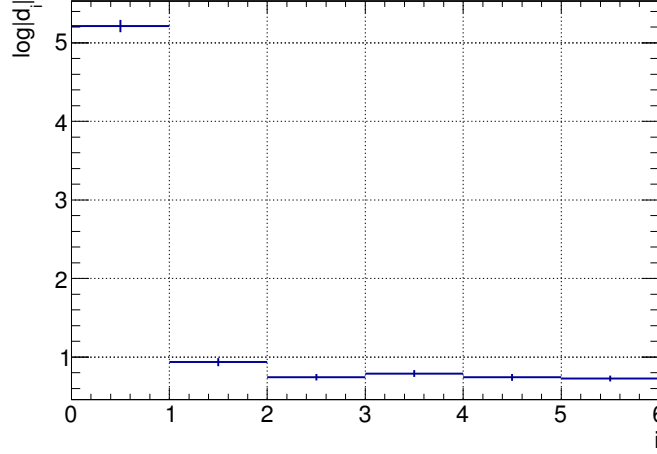


**Figure 4.23:** Trend of the  $\log d_i$  function as a function of  $i$ . The curve flattens for a value  $i = 3$ , used as regularization parameter.

regularization as much as possible until the procedure starts to bias the distribution. The distribution starts to be biased, according to the  $\log d_i$  curve criterion, at  $k_{reg} = 2$ . Looking at figure 4.24, the bias is clearly visible especially for  $k_{reg} = 1$ , when the unfolded distribution does not match anymore the MC truth.

Another test that has been performed consists in unfolding a different distribution using the response matrix built with all the signal samples. The different measured distribution used for this test is obtained considering the VBF sample only. The results are shown in figure 4.25, where the unfolded distribution is compared to MC truth, i.e. VBF sample only, for four different values of the regularization parameter.

The plots show that the unfolded spectrum matches the MC truth only for high values of  $k_{reg}$ , while for lower values the unfolding procedure starts biasing the unfolded distribution, pushing it towards the spectrum used to build the matrix. Of course this is a very extreme situation, where the measured spectrum is far from the expected one.

### 4.10.3 Closure test

A closure test has been performed in order to validate the unfolding procedure. For both gluon fusion and VBF, the samples have been splitted in two equal and statistically independent sets of events: the first set has been used to build the response matrix and the second one to construct the  $p_{T,gen}^H$  distribution after the acceptance cuts only, i.e. the so

called true distribution, and the  $p_{T,\text{reco}}^H$  distribution after the full analysis selection, called measured distribution. The response matrix has then been applied on top of the measured distribution and the unfolded result has been compared with the true histogram. The results are shown in figure 4.26. These plots show a nice agreement between the true histogram and the unfolded one within the uncertainties.

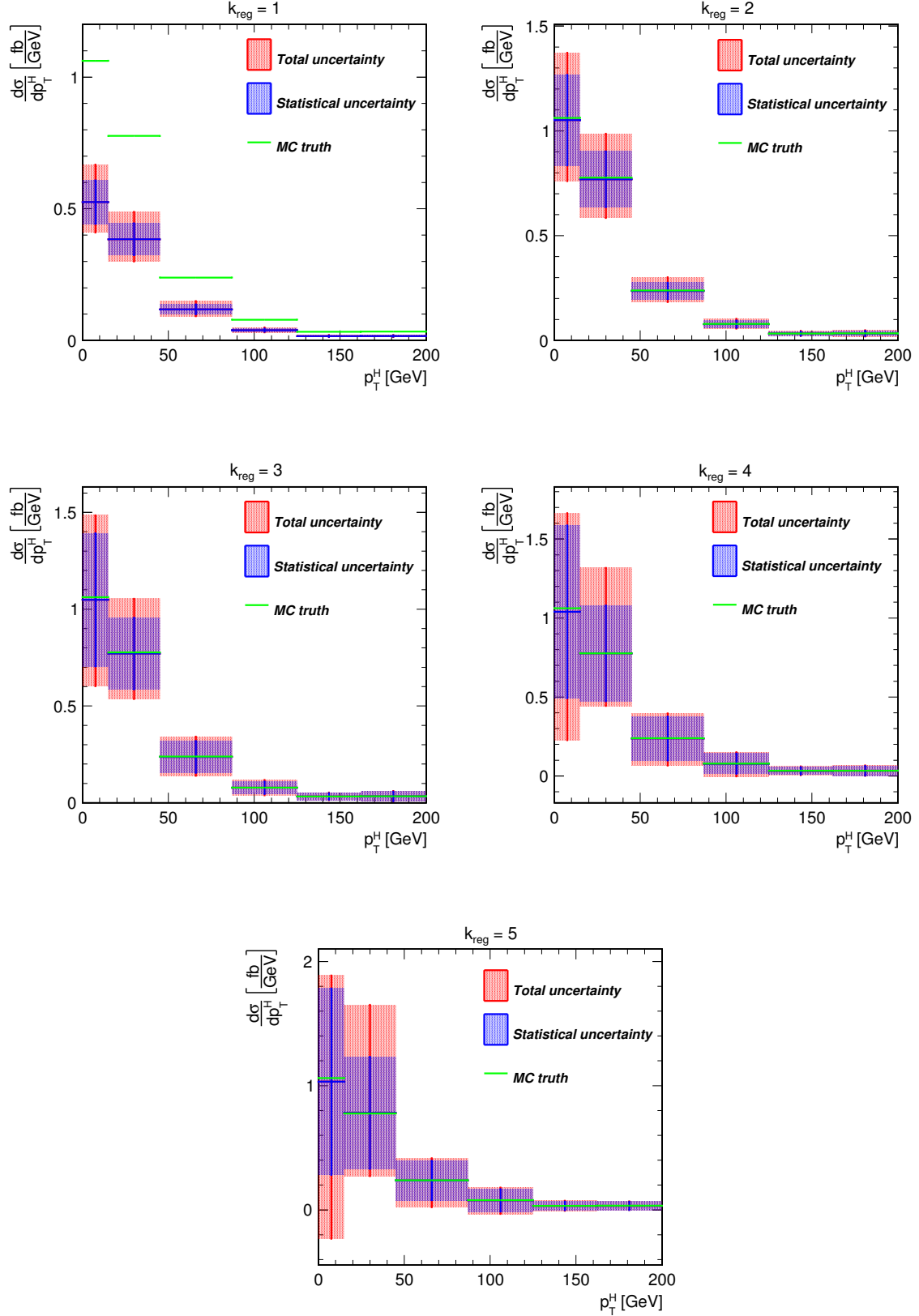
To estimate an uncertainty on the unfolding procedure due to the particular model adopted for building the response matrix we used two independent gluon fusion samples, obtained using two different generators: POWHEG (the default generator used in this analysis) and JHU. A comparison is shown in figure 4.27 between these two gluon fusion samples for the Higgs  $p_T$  spectrum normalized to unity. The JHU gluon fusion sample has been used to build the response matrix and the POWHEG sample to extract the true and the measured histograms to be compared with the unfolded distribution. The results are shown in figure 4.28 and, as can be observed, we have a nice agreement between the true and the unfolded histograms.

As a further cross check we have evaluated the effect of changing the relative fraction of VBF and ggH within the theoretical uncertainty. The test is shown in Fig. 4.29, where three different response matrices, for the nominal, scaled up and scaled down VBF/ggH ratio have been used to unfold the reconstructed level distribution obtained with the nominal VBF/ggH ratio.

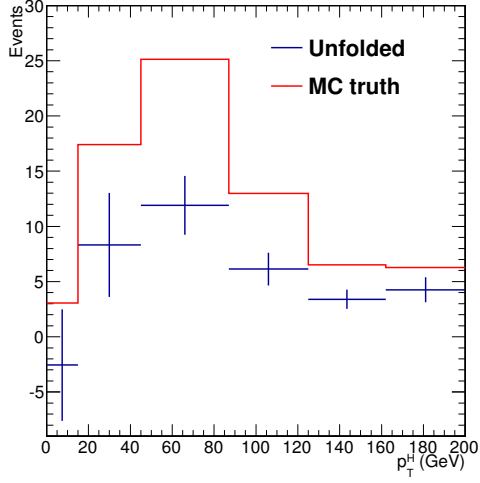
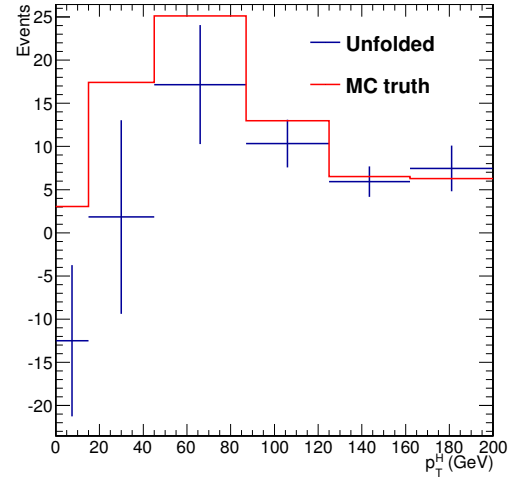
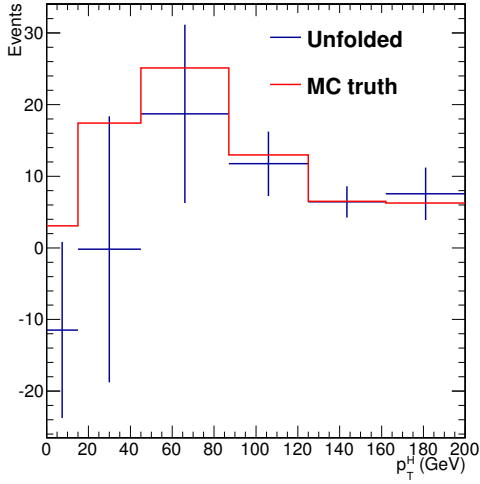
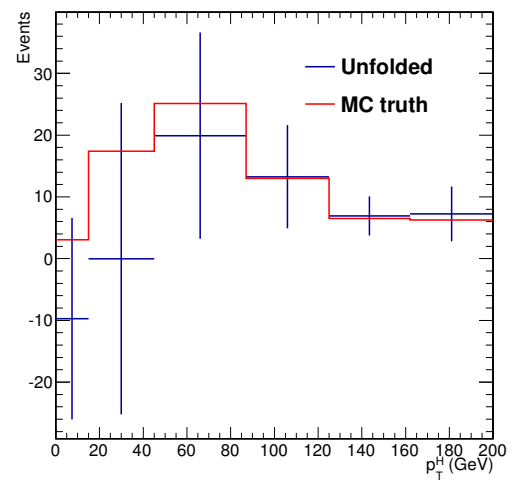
#### 4.10.4 Comparison to ZZ and $\gamma\gamma$ approach

We have followed an unfolding procedure that is different from what has been done in similar differential analyses in ZZ and  $\gamma\gamma$ . In those analyses the correction for bin migration is done at the fit level, by defining the signal according to the truth level binning, rather than the reco-level binning. Then one applies a selection efficiency correction.

We have tried the same approach, obtaining the fit result in Fig. 4.30 (a). The large errors obtained seem to indicate a substantial equivalence between this method and an un-regularized matrix inversion (Fig. 4.30 (b)), although we haven't investigated mathematically this equivalence further. Since our response matrix is significantly non-diagonal, regularization is needed to avoid large statistical errors.



**Figure 4.24:** Unfolded spectrum for several values of the  $k_{reg}$  parameter, from 1 (stronger regularization) to 5 (weaker regularization).

(a)  $k_{reg} = 2$ (b)  $k_{reg} = 3$ (c)  $k_{reg} = 4$ (d)  $k_{reg} = 5$ 

**Figure 4.25:** Unfolded spectrum for several values of the  $k_{reg}$  parameter, from 2 (stronger regularization) to 4 (weaker regularization). The response matrix has been applied on top of a measured distribution containing the VBF signal only.

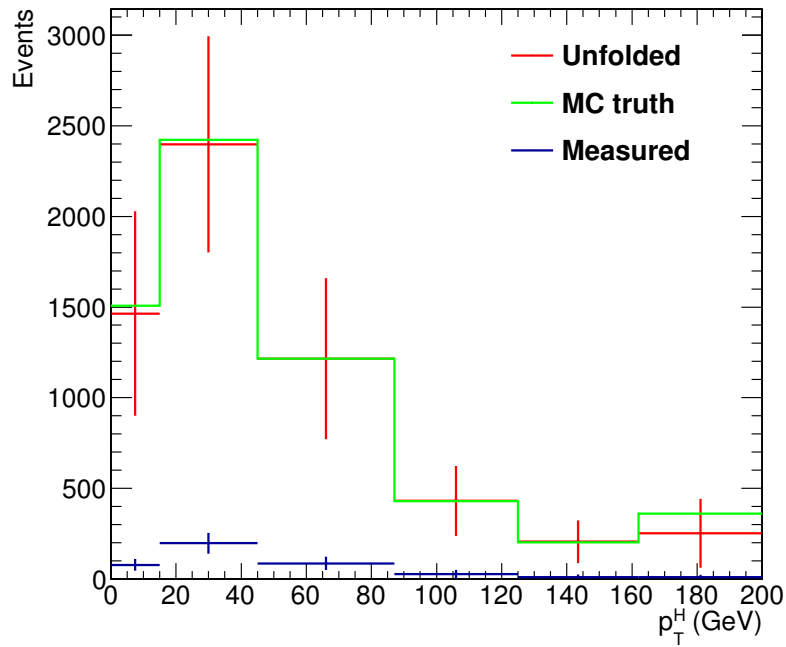


**Figure 4.26:** Comparison among the measured distribution (blue markers), the unfolded distribution (red markers) and MC truth (green line). All signals (ggH, qqH and WZH) are included in the distributions.



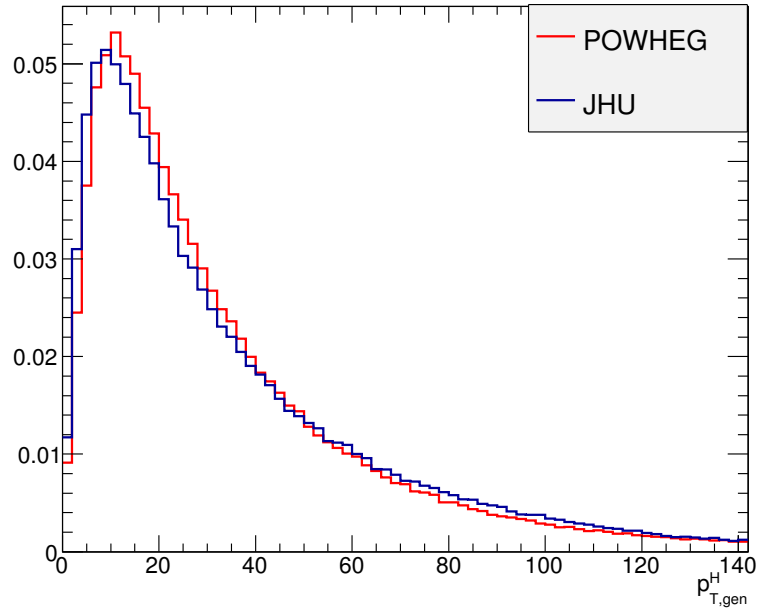


**Figure 4.27:** Comparison between the generator level  $p_T^H$  spectra obtained with POWHEG and JHU for the gluon fusion production mode.

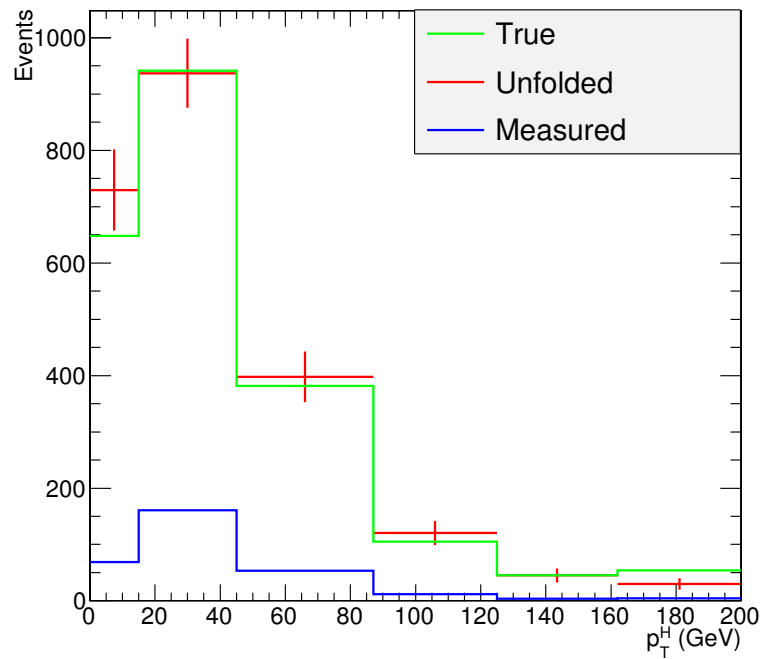


**Figure 4.28:** Closure test in which the JHU ggH sample has been used to build the response matrix and the POWHEG sample to extract the true and measured distributions.

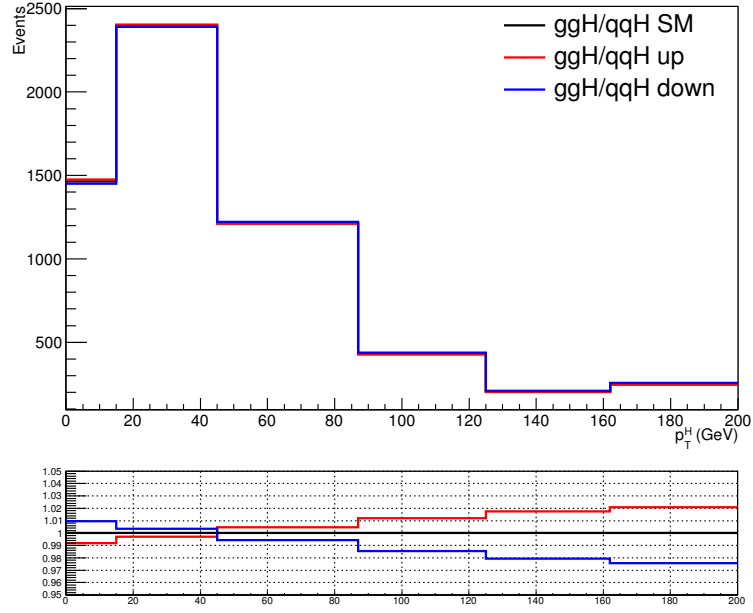


**Figure 4.29:** Unfolded distributions for the nominal  $ggH/VBF$  ratio (black line) and the scaled up (red line) and down (blue line) distributions.

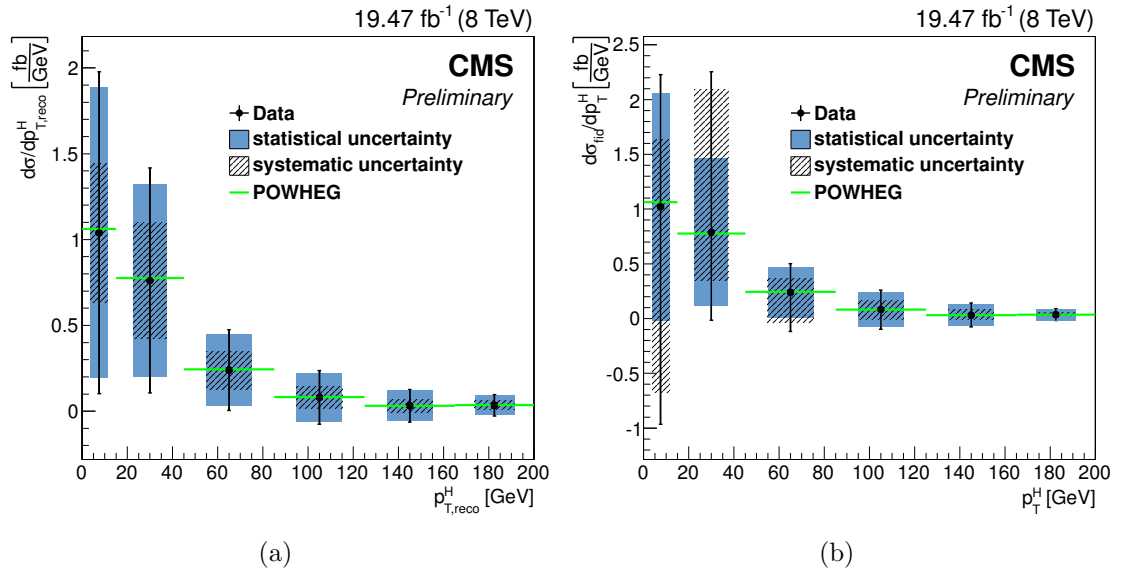


**Figure 4.30:** (a) extraction of the un-smearred signal yields from the fit as in differential  $ZZ$  and  $\gamma\gamma$ . (b) Plain matrix inversion with regular fit.

## 4.11 Uncertainties and Unfolding

Since we plan to unfold the signal yields, we had to carefully understand how the uncertainties propagate through the unfolding. In order to do this we have divided the uncertainties on the extracted signal yields in three categories.

- Uncertainties that only affect the signal yield (type A).
- Uncertainties that affect both the signal yield and the response matrix (type B).
- Uncertainties that affect only the response matrix (type C).

The reason why we had to divide the errors in these three classes is because they are propagated differently through the unfolding procedure. Errors of type A can be extracted from the fit in the form of a covariance matrix, that can be passed to the unfolding machinery as the covariance matrix of the measured distribution. Errors of type B, e.g. the MET scale and resolution, need a special treatment because they not only affect the signal yield, but also affect the response matrix. Finally errors of type C only affect the response matrix, and they represent the dependence of the response matrix on the assumed theoretical model.

### 4.11.1 Type A errors

These uncertainties affect the extracted yield but do not affect the response matrix. A typical example is the background normalization uncertainty. More specifically the nuisances that fall into this category are essentially all background shape and normalization uncertainties. In order to extract from the fit the effect of only these uncertainties we perform a dedicated fit in which all other nuisances but the ones of type A are frozen to their nominal value. We extract from the fit a covariance matrix for the six signal strength parameters that is shown in Fig. 4.31.

In the unfolding procedure, errors of type A included in the measured distribution covariance matrix, are propagated to the unfolded distribution.

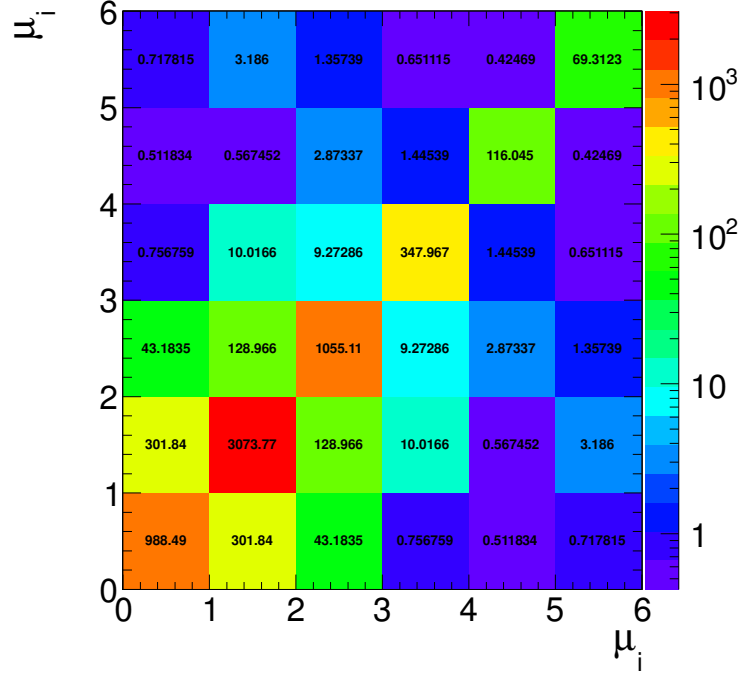


**Figure 4.31:** Covariance matrix for type A nuisances.

#### 4.11.2 Type B errors

These errors affect both the signal strength and the response matrix. The nuisances that fall in this category are:

- the B-veto scale factor (CMS\_8TeV\_btagsf). It affects the signal and background templates by varying the amount of events with jets that enter the selection. It also affects the response matrix because, by varying the fraction of events with jets which are rejected by the veto, it makes the reconstructed spectrum harder or softer.
- The lepton efficiency scale factor (CMS\_8TeV\_eff\_l). It affects the signal and background template shape and normalization. It affects the response matrix by varying the the reconstructed spectrum.
- the MET scale and resolution (CMS\_8TeV\_met, CMS\_8TeV\_p\_scale\_met). The effect is similar to above.
- lepton scale and resolution (CMS\_8TeV\_p\_res\_e, CMS\_8TeV\_p\_scale\_e, CMS\_8TeV\_p\_scale\_m). The effect is similar to above.

- Jet energy scale (CMS\_8TeV\_p\_scale\_j). It affects the signal and background template shape and normalization. It also affects the response matrix because, by varying the fraction of events with jets, the b veto can reject more or less events, thus making the reconstructed spectrum harder or softer.

Since each of these nuisances changes the response matrix in its own way, we cannot extract a global correlation matrix for them, instead we need to evaluate each of them one by one, and then use the varied signal strengths for each of these nuisance in conjunction with the corresponding varied response matrix. In order to evaluate the effect of each of the above mentioned nuisances on the signal strength parameters we have used the following procedure. The first step consists in performing a fit letting all nuisance free to float. Then for each type B nuisance we perform two additional fits: one with the nuisance frozen to a  $+1\sigma$  with respect to its nominal value and one freezing the nuisance to  $-1\sigma$  with respect to its nominal value. The difference on the signal strengths between the two variation and the fit with everything floating gives the uncertainty on the signal strengths due to that particular nuisance. This method allows us also to catch the way in which nuisances are correlated across different  $p_T^H$  bins. The relative errors for each of the type B nuisances is shown in Tab. 4.7. Using these uncertainties, we can build, for each of the type B nuisances, a varied up and a varied down measured spectrum.

For each of the type B nuisances we also build an up and a down varied response matrix. For each type B nuisance we can thus build an unfolded varied up and varied down spectrum, simply by applying the unfolding to the varied spectrum using the corresponding varied response matrix.

## Likelihood scans

In order to further validate the numbers reported in the table 4.7 and to verify the goodness of the fitting procedure, a scan of the likelihood function has been performed using a grid of points in a two-dimensional space.

In the following, a nuisance value of 0 corresponds to its nominal value while the  $\pm 1\sigma$  variations correspond exactly to  $\pm 1$  values.

The scan has been performed in the nuisance/signal strength space for some correlated nuisances and for all the  $p_T^H$  bins, taking the nuisance and the signal strength as parameters of interest. For each parameters of interest/nuisance pair a 10000 points grid scan of the

**Table 4.7:** Effect of all the correlated nuisances on the signal strengths of each bin. In the table are reported the signal strength variations corresponding to an up or down scaling of the nuisance.

nuisance	bin1	bin2	bin3	bin4	bin5	bin6
CMS-8TeV_btagsf	-10.1/-8.8 (%)	7.3/12.2 (%)	-6.3/3.1 (%)	-14.4/-4.8 (%)	-5.4/14.5 (%)	-7.9/17.8 (%)
CMS-8TeV_eff1	-14.7/-3.9 (%)	4.5/15.1 (%)	-5.7/2.5 (%)	-13.2/-5.3 (%)	-0.2/7.6 (%)	-0.1/6.8 (%)
CMS-8TeV_met	-12.5/0.0 (%)	15.4/-0.0 (%)	-12.8/-0.0 (%)	8.7/0.0 (%)	-20.9/-0.0 (%)	10.5/0.0 (%)
CMS-8TeV_p_res-e	-12.5/-0.0 (%)	11.2/0.0 (%)	-2.4/0.0 (%)	-13.4/-0.0 (%)	9.9/0.0 (%)	-4.6/-0.0 (%)
CMS-8TeV_p-scale-e	-2.7/-13.1 (%)	15.9/9.9 (%)	10.8/-16.8 (%)	16.2/-33.1 (%)	30.9/-14.4 (%)	12.6/-10.9 (%)
CMS-8TeV_p-scale-j	-10.9/-10.1 (%)	9.0/9.0 (%)	-3.0/-2.9 (%)	-10.3/-8.9 (%)	0.3/3.4 (%)	5.2/3.1 (%)
CMS-8TeV_p-scale-m	-7.0/-10.7 (%)	11.8/8.9 (%)	1.1/-8.7 (%)	-0.7/-14.4 (%)	14.5/-4.6 (%)	8.0/-1.6 (%)
CMS-8TeV_p-scale-met	-14.4/-6.8 (%)	-0.0/17.7 (%)	-6.1/-7.1 (%)	9.6/-20.9 (%)	2.3/32.4 (%)	2.5/2.6 (%)

likelihood function is performed. In this way a two-dimensional likelihood scan is obtained. To verify the numbers in table 4.7 the two-dimensional likelihood plot has been divided in several slices and the one-dimensional likelihood slice corresponding to the upper and lower variation of the nuisance, i.e.  $nuisance = 1$  or  $nuisance = -1$  respectively, are shown as a function of the signal strength of a given bin.

In this way we can determine if the likelihood function has a reasonable trend and if the minimum corresponds to the value shown in the table.

In figures 4.32 and 4.33 are reported the two-dimensional scans and the corresponding  $\pm 1\sigma$  profiles for the b-tagging nuisance in each  $p_T^H$  bin. The scans have been performed varying the nuisance in the range from  $-2$  to  $+2$  and the signal strengths from  $0$  to  $+2$ . All the scans show the expected trend and the minimum points of the profiles, pointed out by dashed vertical lines, correspond to the numbers in the correlated systematics table.

In figures 4.34 and 4.35 are shown the same plots but, in this case, scanning the lepton efficiency nuisance.

### 4.11.3 Type C errors

Type C errors are those that only change the response matrix. They can be modeled with alternative response matrices that can be used to unfold the central fit result. A way to evaluate type C effects is the one depicted in Sec. 4.10.3, i.e. either by taking an alternative model for  $p_T^H$ , or by varying the VBF/ggH ratio. It is important to note the either of those variations (JHU vs Powheg or variation of VBF/ggH) does not affect the shape of the signal templates, so it only affects the response matrix, and not the signal extraction.

We have checked that this is the case by comparing in shape the ggH and VBF templates in in each  $p_T^H$  bin. The comparison for  $m_{\ell\ell}$  is shown in Fig. 4.36. The differences are within the statistical accuracy of the samples.

In order to assess whether the uncertainty on the VBF/ggH ratio has an effect on the signal extraction we have run three comparisons.

1. We have run 2000 MC toys for the full backgrounds+ggH+VBF expected spectra and we have fitted the signal yield in each bin both with the full ggH+VBF and with the ggH only template. The comparison is shown in Fig. 4.37 (a).

2. We have run 2000 MC toys for the backgrounds+ggH spectra and we have fitted the signal yield in each bin both with the ggH only template and with the VBF only template. The comparison is shown in Fig. 4.37 (b).
3. We have run 2000 MC toys for the backgrounds+VBF (times 10) spectra and we have fitted the signal yield in each bin both with the VBF only template and with the ggH only template. The comparison is shown in Fig. 4.37 (c).

#### **4.11.4 Combination of errors of different type**

In order to combine errors of type A, B and C after the unfolding we follow the following recipe: we sum in quadrature positive and negative errors separately, thus we obtain possibly asymmetric error bars. In case of type B errors that go in the same direction for both the up and the down variation, we propagate the maximum variation.



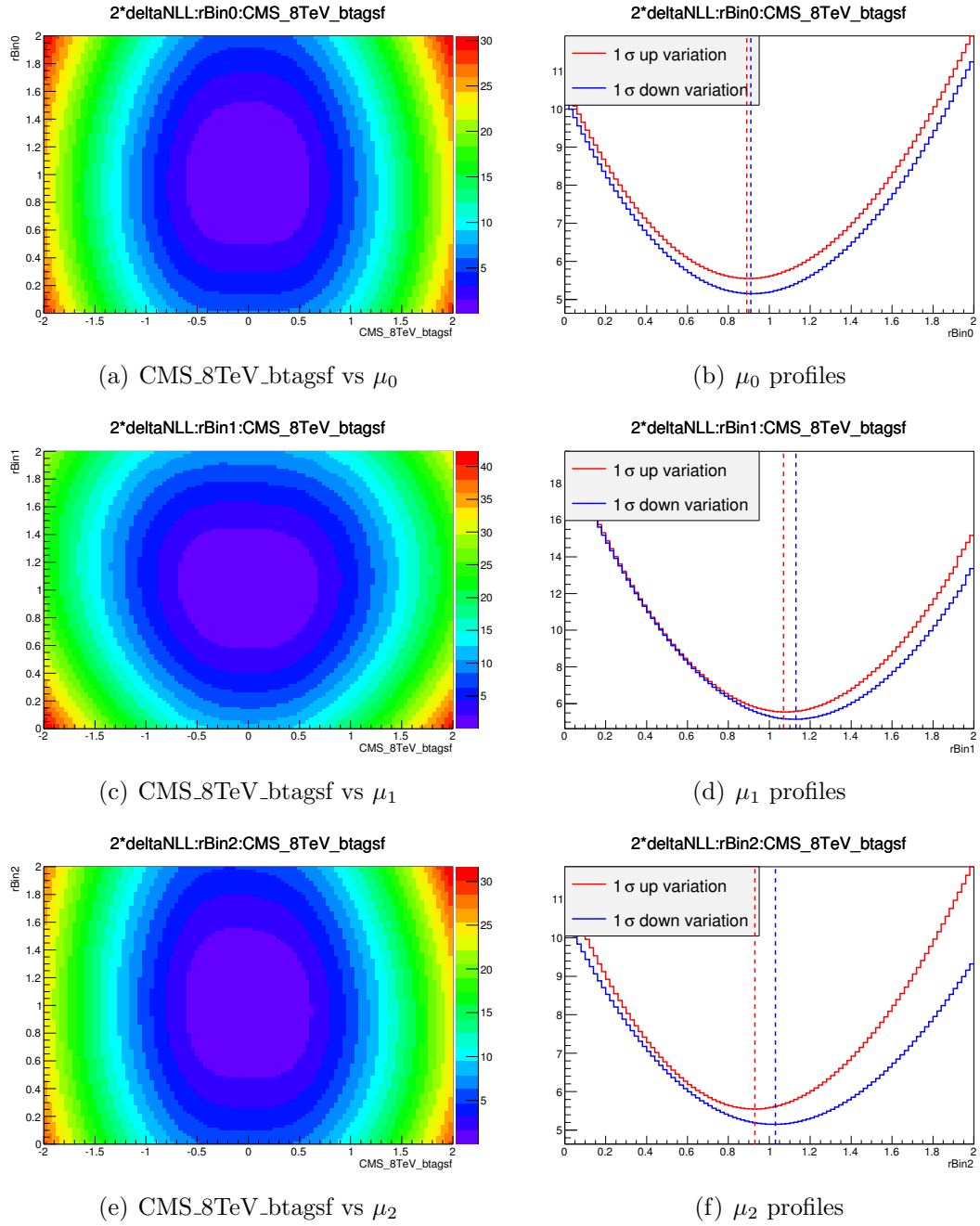


**Figure 4.32:** **Left side** Two-dimensional likelihood scan for b-tagging nuisance vs signal strengths in several bins: (a) bin 0, (c) bin 1, (e) bin 2. **Right side** Likelihood profiles corresponding to the nuisance  $\pm 1\sigma$  up/down variations for (b) bin 0, (d) bin 1 and (f) bin 2.

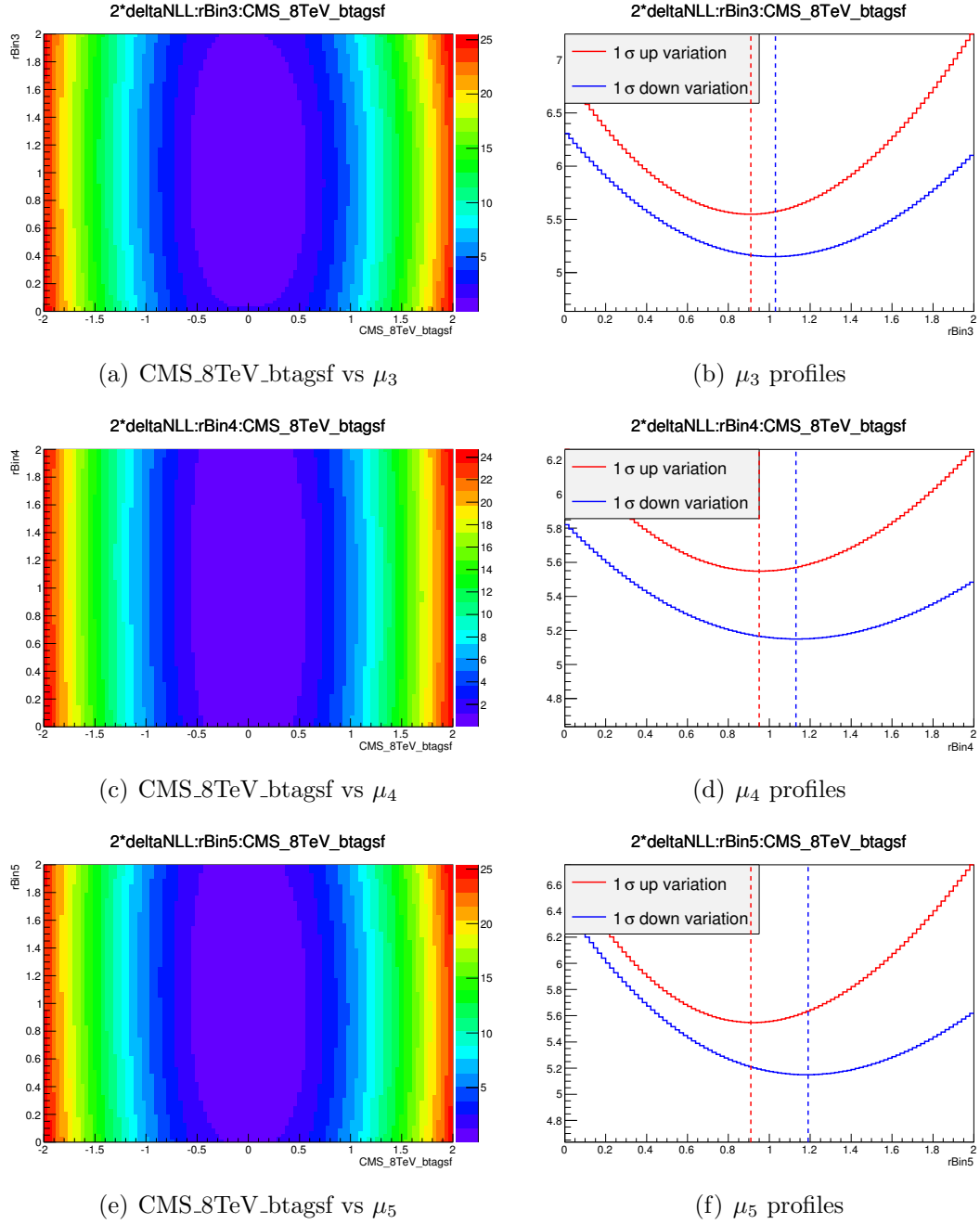


**Figure 4.33:** **Left side** Two-dimensional likelihood scan for b-tagging nuisance vs signal strengths in several bins: (a) bin 3, (c) bin 4, (e) bin 5. **Right side** Likelihood profiles corresponding to the nuisance  $\pm 1\sigma$  up/down variations for (b) bin 3, (d) bin 4 and (f) bin 5.

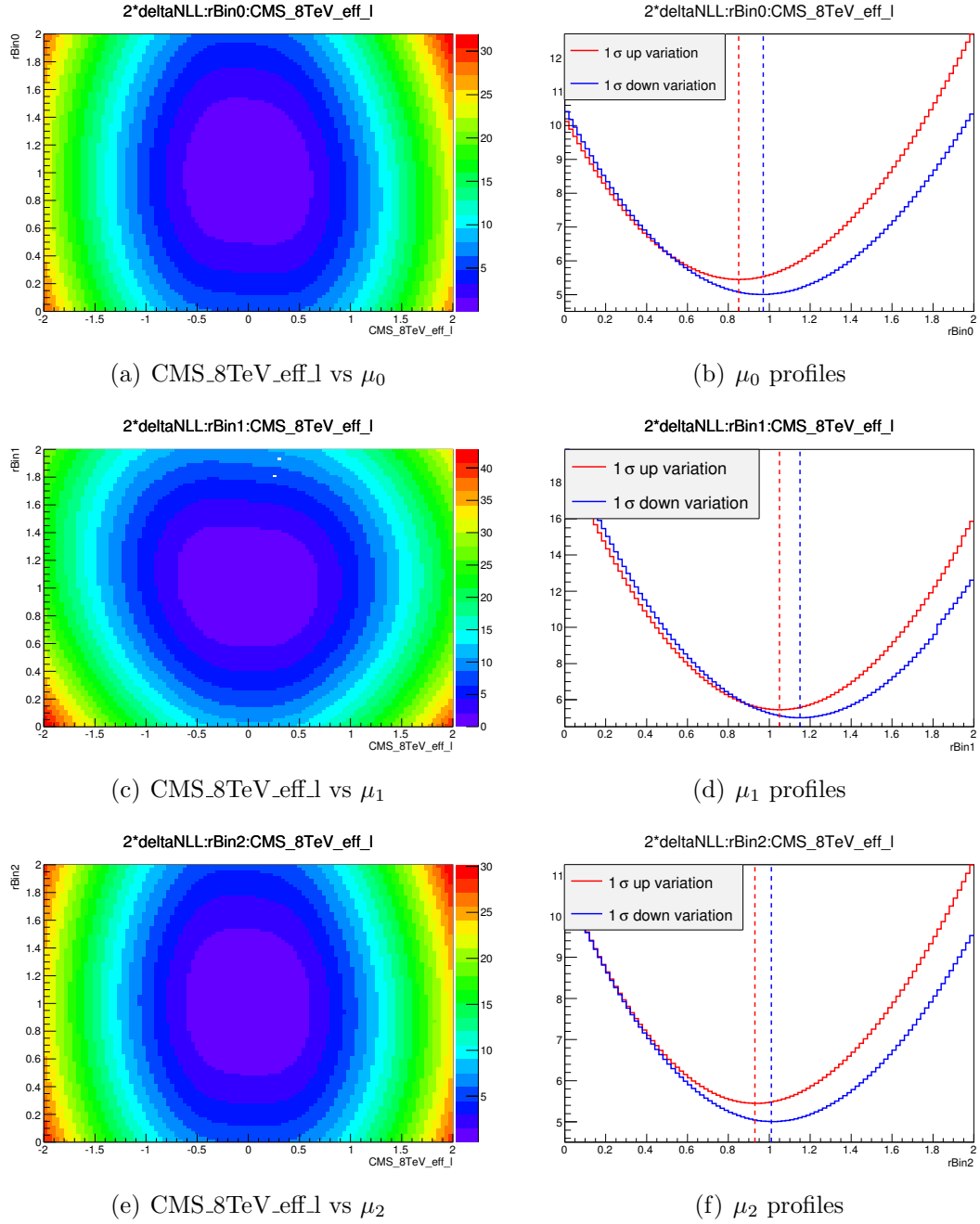


**Figure 4.34:** **Left side** Two-dimensional likelihood scan for lepton efficiency nuisance vs signal strengths in several bins: (a) bin 0, (c) bin 1, (e) bin 2. **Right side** Likelihood profiles corresponding to the nuisance  $\pm 1\sigma$  up/down variations for (b) bin 0, (d) bin 1 and (f) bin 2.

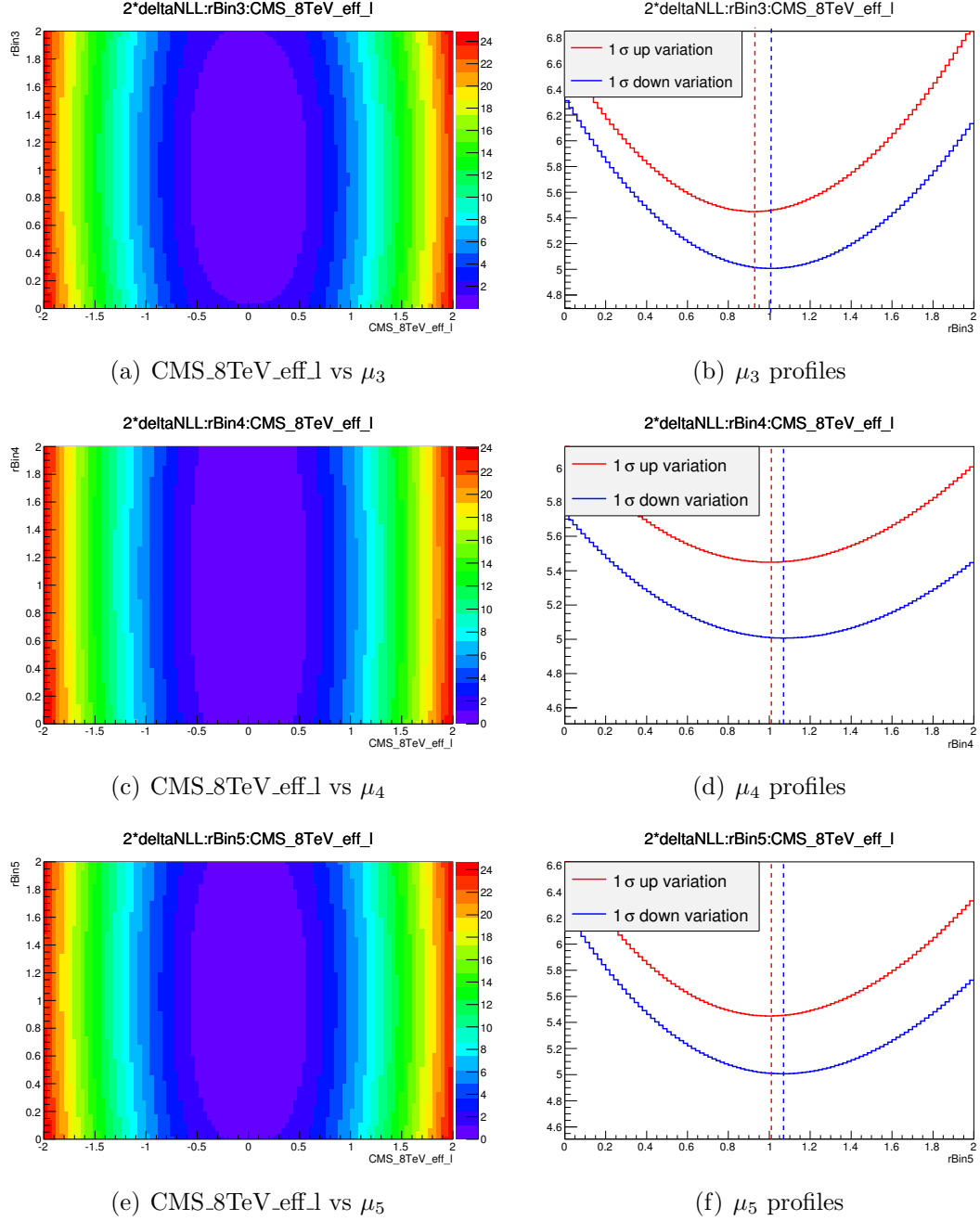


**Figure 4.35:** **Left side** Two-dimensional likelihood scan for lepton efficiency nuisance vs signal strengths in several bins: (a) bin 3, (c) bin 4, (e) bin 5. **Right side** Likelihood profiles corresponding to the nuisance  $\pm 1\sigma$  up/down variations for (b) bin 3, (d) bin 4 and (f) bin 5.

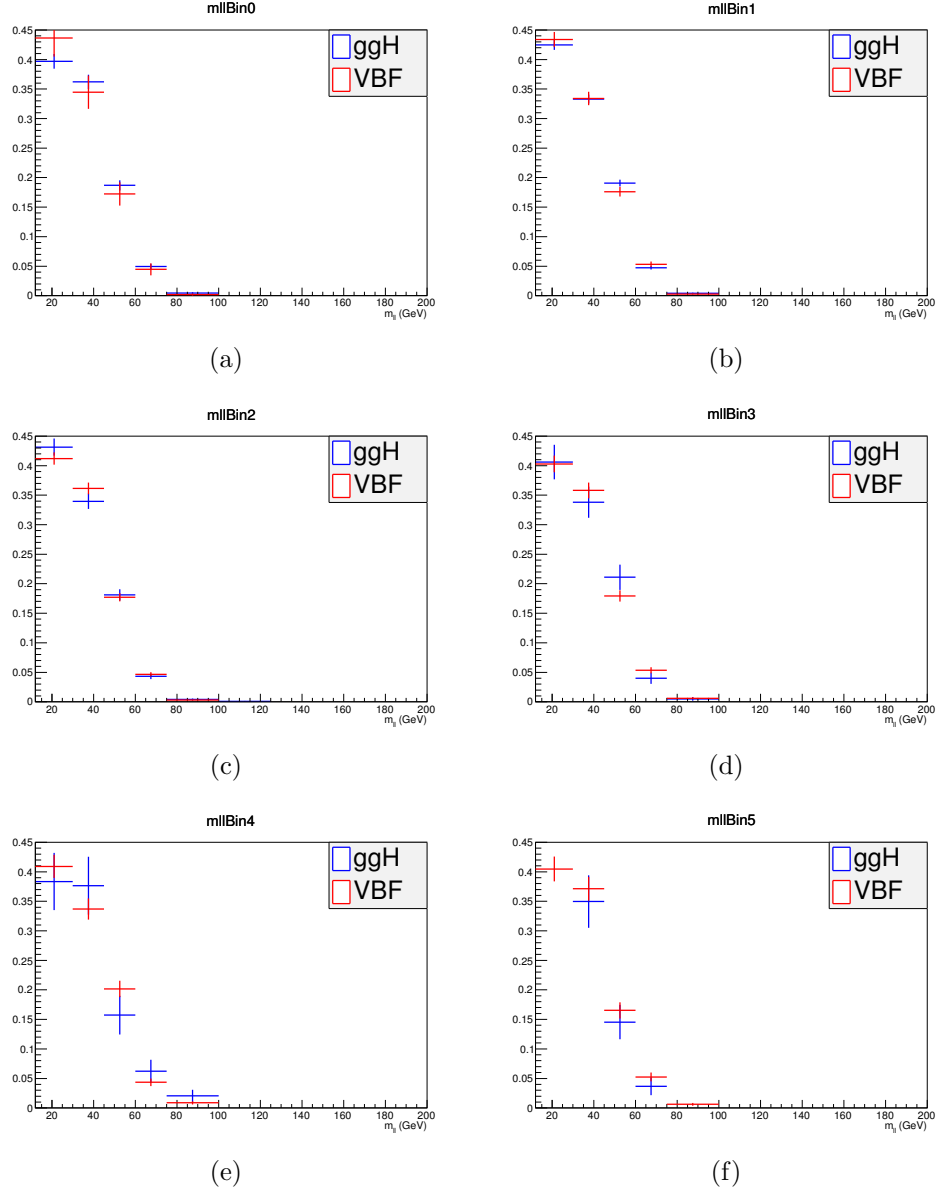
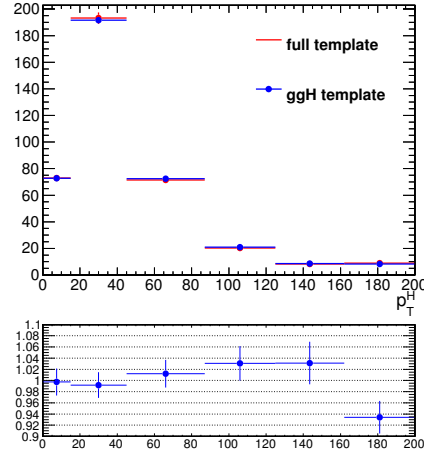
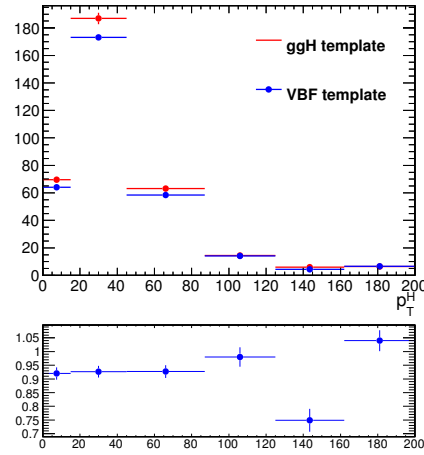


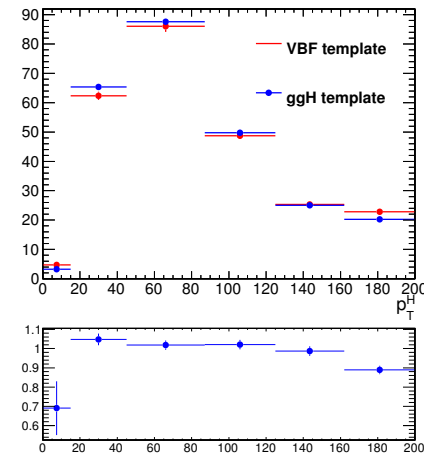
**Figure 4.36:** Comparison of  $m_{\ell\ell}$  template shapes in ggH and VBF samples.



(a)



(b)



(c)

**Figure 4.37:** Signal yields extracted with different templates in the  $m_{\ell\ell}$ - $m_T$  plane. (a) average of 2000 toys produced with the full backgrounds+ggH+VBF template and fitted either with full ggH+VBF templates for  $m_{\ell\ell}$ - $m_T$  or with the ggH only  $m_{\ell\ell}$ - $m_T$  templates. (b) average of 2000 toys produced with the full backgrounds+ggH template and fitted either with ggH templates for  $m_{\ell\ell}$ - $m_T$  or with the VBF only  $m_{\ell\ell}$ - $m_T$  templates. (c) average of 2000 toys produced with the full backgrounds+VBF (times 10) template and fitted either with VBF templates for  $m_{\ell\ell}$ - $m_T$  or with the

## 4.12 Results

Once the signal strengths are extracted from the fit results, as explained in section 4.9, and the uncertainties are decoupled the categories depicted in section 4.11, i.e. type A and type B uncertainties, we can go on unfolding the measured spectrum. In figure 4.38 is shown the  $p_{T,\text{reco}}^H$  differential distribution before applying the unfolding procedure, compared with the MC truth expectation. The corresponding numbers are reported in table 4.8.

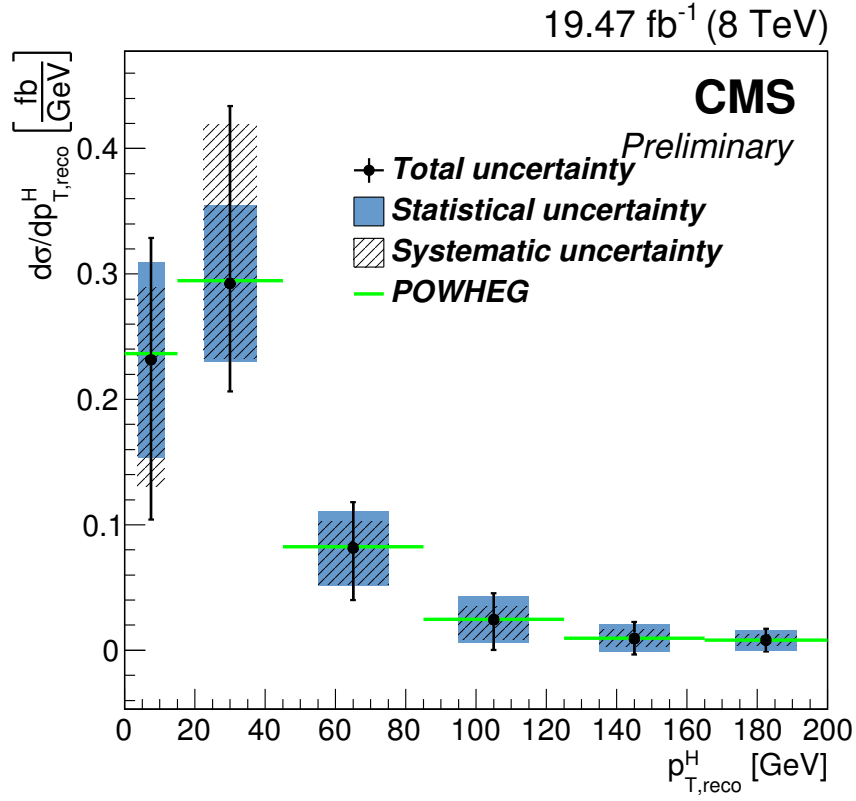


**Figure 4.38:** Differential Higgs production cross section as a function of  $p_{T,\text{reco}}^H$  before applying the unfolding procedure. The bins content corresponds to the MC prediction since the fit is performed on an Asimov dataset. The MC truth is represented by the green line.

In order to unfold the spectrum, the procedure described in section 4.10 has been pursued. The statistical plus type A systematic uncertainties are correctly propagated by the unfolding procedure into the final spectrum, taking into account the signal strengths covariance matrix. The type B systematic uncertainty has been propagated using the following procedure: for each  $p_T^H$  bin, we compute the upper bound of the systematic band

**Table 4.8:** Measured values for each bin of  $p_T^H$  with the corresponding total uncertainty compared with the MC truth expectation.

Bin	Unfolded value	Total error(%)	Stat error(%)	Syst error(%)	MC truth
1	0.23	+41.9/-55.0	$\pm 33.6$	+25.0/-43.5	0.24
2	0.30	+48.3/-29.5	$\pm 21.3$	+43.3/-20.4	0.30
3	0.08	+44.8/-50.9	$\pm 36.5$	+26.1/-35.4	0.08
4	0.02	+88.1/-99.1	$\pm 75.9$	+44.8/-63.8	0.02
5	0.01	+141.1/-135.2	$\pm 116.3$	+80.0/-68.9	0.01
6	0.01	+112.9/-110.6	$\pm 99.5$	+53.3/-48.4	0.01

computing the square sum of all the signal strength variations that deviate in the up direction with respect to the bin central value, whether or not this variation corresponds to the up or down shift of the nuisance. The same is done for the lower bound of the systematic band. If both the up and down shifts of a given nuisance lead to a same direction variation of the signal strength, only the larger variation is considered.

Results are reported in terms of a differential distribution, dividing by the luminosity (the uncertainty on the luminosity measurement is included in the statistical error band), and putting in each bin the bin content divided by the bin width.

In figure 4.39 is shown the Higgs differential production cross section as a function of  $p_T^H$ . The results reported in this plot have been extracted fitting an Asimov dataset, thus the bins content corresponds to what expected from the MC predictions. The red shaded area in each bin represents the total uncertainty due to statistics plus systematics (type A and B). The blue area corresponds to the statistical error only. Data are not shown since the analysis is still blinded. As a cross check, the MC truth prediction has been superimposed to the plot. The final results are also shown in table 4.9. The systematic error reported in the table has been extracted in each bin by taking the difference of the squares of total and statistical error.

A comparison between pre-unfolding and unfolded distributions shows that the relative uncertainties in each bin get reduced after the unfolding. To check the correctness of this result, a test using MC toys has been performed and is explained in Appendix ??.

Together with the unfolded spectrum, also the covariance matrix of the six bins is reported, in order to assess how much different bins are correlated. The result is shown in figure 4.40.



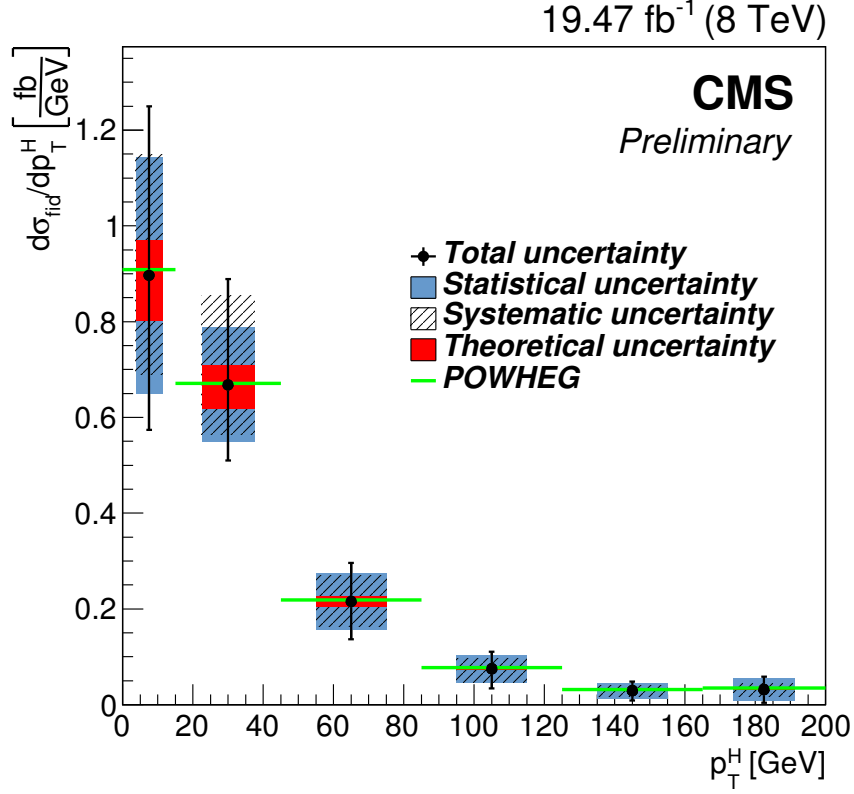


**Figure 4.39:** Unfolded differential Higgs production cross section as a function of  $p_T^H$ . The bins content corresponds to the MC prediction since the fit is performed on an Asimov dataset. The error bars are the total expected uncertainties in this measurement. Also the statistical, the systematic and the theoretical uncertainties are shown separately. The MC truth (POWHEG) is represented by the green histogram.

The differential spectrum can be integrated to obtain a measurement of the inclusive cross section inside the fiducial region. The uncertainties can be correctly taken into account in this calculation using the covariance matrix of the six signal strengths to propagate the errors. In this case the unfolding procedure is not needed and to extrapolate the measured result to the fiducial region, only the efficiency of the analysis selection is needed.

The measured cross section after the analysis selection, i.e. number of events divided by luminosity, is  $14 \pm 4$  fb. Using the overall efficiency defined in section 4.4.2, i.e.  $\epsilon = 0.362 \pm 0.005$ , the cross section value in the fiducial region can be determined and is

**Table 4.9:** Unfolded values for each bin of  $p_T^H$  with the corresponding total uncertainty compared with the MC truth expectation.

Bin	Unfolded value	Total error(%)	Stat error(%)	Syst error(%)	MC truth
1	0.23	+42.4/-55.4	$\pm 34.0$	+25.3/-43.7	0.24
2	0.29	+48.7/-30.0	$\pm 21.5$	+43.6/-20.9	0.29
3	0.08	+45.7/-51.9	$\pm 36.9$	+26.9/-36.4	0.08
4	0.02	+88.5/-99.5	$\pm 76.1$	+45.2/-64.1	0.02
5	0.01	+141.3/-135.3	$\pm 116.4$	+80.1/-69.0	0.01
6	0.01	+112.9/-110.6	$\pm 99.5$	+53.4/-48.4	0.01

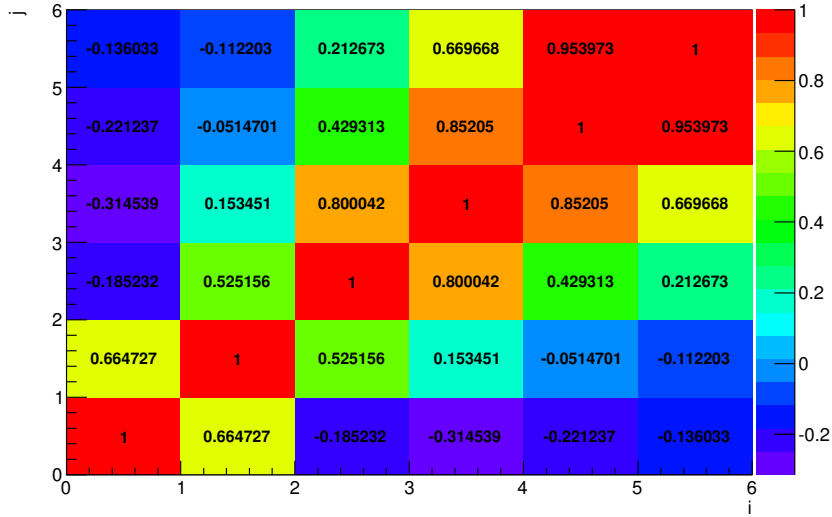


**Figure 4.40:** Covariance matrix of the six  $p_T^H$  bins related to the unfolded distribution.

equal to:

$$\sigma_{fid} = 47 \pm 7 \text{ (stat)} \pm 9 \text{ (syst)} \text{ fb} \quad . \quad (4.21)$$

As a closure test, the measurement can be extrapolated to the full  $4\pi$  acceptance, using the efficiency reported in section 4.4.2, which is  $\epsilon = 0.03960 \pm 0.00033$ . The resulting cross section is:

$$\sigma_{4\pi} = 433 \pm 67 \text{ (stat)} \pm 83 \text{ (syst)} \text{ fb} \quad , \quad (4.22)$$

in agreement with the expected value from MC.



# Chapter 5

## First $H \rightarrow WW$ results at 13 TeV

### 5.1 Higgs boson search at 13 TeV

### 5.2 Search for a high mass resonance in the $WW$ decay channel at 13 TeV

### 5.3 Conclusions









# Bibliography

- [1] Serguei Chatrchyan et al. “Measurement of Higgs boson production and properties in the WW decay channel with leptonic final states”. In: *JHEP* 01 (2014), p. 096. DOI: 10.1007/JHEP01(2014)096. arXiv: 1312.1129 [hep-ex].
- [2] J. Brochero *et al.* “Higgs Boson Decaying to WW in the Leptonic Final State using 2011 and 2012 Data”. In: *CMS Note* AN-2013/022 (2013).
- [3] J. Brochero *et al.* “Search for a Standard Model Higgs boson produced via Vector Boson Fusion, in the decay channel  $H \rightarrow WW \rightarrow l\nu l\nu$  using 2011 and 2012 data”. In: *CMS Note* AN-2013/097 (2013).
- [4] L. Bauerdick *et al.* “A Higgs Boson Search in the Fully Leptonic W+W- Final State (update for ICHEP2012 conference)”. In: *CMS Note* AN-2012/228 (2012).
- [5] L. Bauerdick *et al.* “A Higgs Boson Search in the Fully Leptonic W W Final State”. In: *CMS Note* AN-2013/052 (2013).
- [6] S. Frixione, P. Nason and C. Oleari. “Matching NLO QCD computations with Parton Shower simulations: the POWHEG method”. In: *arXiv:0709.2092v1* (2007).
- [7] J. Alwall *et al.* “Madgraph”. In: *JHEP* 0709 (2007), p. 028.
- [8] T. Sjostrand, S. Mrenna and P. Skands. “PYTHIA”. In: *JHEP* 0605 (2006), p. 026.
- [9] Hung-Liang Lai et al. “Uncertainty induced by QCD coupling in the CTEQ global analysis of parton distributions”. In: *Phys. Rev. D* 82 (2010), p. 054021. DOI: 10.1103/PhysRevD.82.054021. arXiv: 1004.4624 [hep-ph].
- [10] Huang-Liang Lai et al. “New parton distributions for collider physics”. In: *Phys. Rev. D* 82 (2010), p. 074024. DOI: 10.1103/PhysRevD.82.074024. arXiv: 1007.2241 [hep-ph].
- [11] S. Agostinelli et al. “GEANT4: A simulation toolkit”. In: *Nucl. Instrum. Meth. A* 506 (2003), p. 250. DOI: 10.1016/S0168-9002(03)01368-8.

- [12] J. Brochero *et al.* “Search for the Higgs Boson Decaying to WW in the Fully Leptonic Final State at 8 TeV”. In: *CMS Note* AN-2012/194 (2012).
- [13] CMS collaboration. *Search for associated Higgs boson production (VH) with  $H \rightarrow W^+W^- \rightarrow \ell\nu\ell\nu$  and hadronic V decay in pp collisions at  $\sqrt{s} = 7$  TeV and 8 TeV*. CMS PAS 2013/084. 2013. URL: <http://cds.cern.ch/record/1560844>.
- [14] CMS collaboration. *WW Cross Section Measurement at  $\sqrt{s} = 8$  TeV*. CMS AN 2014/056. 2014.
- [15] H. Bakhshian et al. “Computing the contamination from fakes in leptonic final states”. In: *CMS Note* AN-2010/261 (2010).
- [16] H. Bakhshian et al. “Lepton fake rates in dilepton final states”. In: *CMS Note* AN-2010/397 (2010).
- [17] J. Brochero *et al.* “Higgs Boson Decaying to WW in the Fully Leptonic Final State”. In: *CMS Note* AN-2012/378 (2012).
- [18] M. Bluj, *et al.* “Modelling of tautau final states by embedding tau pairs in Z to mumu events”. In: *CMS Note* (2011).
- [19] CMS Collaboration. “Evidence for a particle decaying to W+W- in the fully leptonic final state in a standard model Higgs boson search in pp collisions at the LHC”. In: *Hig12042 Twiki* (2012). URL: [https://twiki.cern.ch/twiki/bin/view/CMSPublic/Hig12042TWiki#Study\\_on\\_W\\_g\\_background](https://twiki.cern.ch/twiki/bin/view/CMSPublic/Hig12042TWiki#Study_on_W_g_background).
- [20] CMS Collaboration. “Standard Model Cross Sections for CMS at 7 TeV”. In: *CMS Generator Group Twiki* (2010).
- [21] John M. Campbell, R. Keith Ellis, and Ciaran Williams. “Vector boson pair production at the LHC”. In: *JHEP* 07 (2011), p. 018. DOI: 10.1007/JHEP07(2011)018. arXiv: 1105.0020 [hep-ph].
- [22] J. Ohnemus. “Order alpha-s calculations of hadronic W+- gamma and Z gamma production”. In: *Phys. Rev. D* 47 (1993), pp. 940–955. DOI: 10.1103/PhysRevD.47.940.
- [23] JetMET group. “Jet energy uncertainties, [https://twiki.cern.ch/twiki/bin/view/CMS/JECUncertaintySources#2012\\_JEC](https://twiki.cern.ch/twiki/bin/view/CMS/JECUncertaintySources#2012_JEC)”. In: (). URL: [https://twiki.cern.ch/twiki/bin/view/CMS/JECUncertaintySources%5C#2012\\_JEC](https://twiki.cern.ch/twiki/bin/view/CMS/JECUncertaintySources%5C#2012_JEC).
- [24] *Procedure for the LHC Higgs boson search combination in Summer 2011*. Tech. rep. CMS-NOTE-2011-005. ATL-PHYS-PUB-2011-11. Geneva: CERN, Aug. 2011.

- [25] Tim Adye. “Unfolding algorithms and tests using RooUnfold”. 2011.
- [26] Glen Cowan. *Statistical Data Analysis*. Oxford University Press, Oxford, 1998.
- [27] Andreas Hocker and Vakhtang Kartvelishvili. “SVD approach to data unfolding”. In: *Nucl. Instrum. Meth. A* 372 (1996), p. 469. DOI: 10.1016/0168-9002(95)01478-0. arXiv: hep-ph/9509307 [hep-ph].

